Experimental Studies on Creping and Its Influence on Mechanical Properties of Tissue Paper Products

by

Ratul Das

B.Tech., Indian Institute of Technology Roorkee, 2016

A THESIS SUBMITTED IN PARTIAL FULFILMENT OF
THE REQUIREMENTS FOR THE DEGREE OF

Master of Applied Science

in

The Faculty of Graduate and Postdoctoral Studies

(Mechanical Engineering)

The University of British Columbia

(Vancouver)

January 2019

The following individuals certify that they have read, and recommend to the Faculty of Graduate and Postdoctoral Studies for acceptance, a thesis/dissertation entitled:

Experimental Studies on Creping and Its Influence on Mechanical Properties of Tissue Paper Products

submitted by   Ratul Das   in partial fulfillment of the requirements for

the degree of   Master of Applied Science

in   Mechanical Engineering

Examining Committee:

Dr. A. Srikantha Phani
Co-supervisor

Dr. Sheldon Green
Co-supervisor

Dr. Gary S. Schajer
Supervisory Committee Member

Dr. Mauricio Ponga
Supervisory Committee Member

Abstract

Tissue papers are softer, stretchier, and more water absorbent than regular writing or packaging paper products. Creping of an adhesively bonded low-density paper web from the surface of a rotating Yankee drum is the key manufacturing technique in tissue production. Creping densifies and weakens the paper by partially damaging the fibers and the inter-fiber bonds in the fiber network. The process also imparts a signature microstructure, called crepe structure, to the tissue paper. Tissues thus produced have a high specific volume (bulk to basis weight ratio), work to rupture, failure strain (stretch), softness and absorbency. Mechanical properties of tissues are governed by the creping process. Therefore, a scientific understanding of the creping process, and its impact on the structural and mechanical properties of the tissue paper is important.

The present research approaches the highly complex problem from an experimental perspective, with a view to complement ongoing physics based numerical models to simulate creping. Experimental techniques are developed to visualize the high speed creping process, quantify the crepe structure, and finally understand the influence of the crepe structure on the uni-axial tensile response of the tissue. A novel surface imaging based structural quantification technique is developed and successfully demonstrated on a commercial tissue machine. The surface image based quantification technique is also validated by micrographic observations of the tissue cross section under a Scanning Electron Microscope (SEM). This work lays the foundational techniques and protocols for future studies in the laboratory and opens the opportunity to observe crepe structure in real time for quality and process control.

The surface imaging techniques are then used to observe the evolution of the creping microstructure under a tensile load. Local two dimensional strain fields are quantified using Digital Image Correlation (DIC) to gain insight into failure mechanisms at the macroscopic network level. Micro tensile tests are conducted under SEM to gain further insight into the deformation and failure mechanisms operative at fiber length scales. The studies showed the impact of the creping structure, formation, and inter fiber bonds on the tensile response of the tissue paper, specifically along machine direction.

Lay Summary

Tissue paper is a complex material. During tissue manufacture, pulp is first dried on a chemical-coated rotating drum until it is 95 percent dry. It is then pushed off at very high speed by a sharp creping blade, creating hundreds of microscopic folds that give tissue its softness, flexibility, tearing resistance and strength. To scientifically understand how the creping folds affect a tissue paper is a top concern for the paper industry. This research aims to quantify the creping folds and relate them to the tissue properties. A novel surface image based creping fold measurement system is developed. This enables process monitoring on a tissue machine. The visualization technique is then used to observe and analyze the change in tissue micro-structure under load. This research offers insight into the quantification of creping structure and its influence on mechanical properties of tissue papers.

Preface

Parts of Chapter 2 and Chapter 4 of this thesis have been included in a research paper [1] : "An Elastoplastic Creping Model for Tissue Manufacturing". The paper is under review for publication in International Journal of Solids and Structures.

In Chapter 2, the Line Laser and surface imaging setup are designed by the author in the Dynamics and Applied Mechanics Lab at The University of British Columbia. Sample preparation for Scanning Electron Microscope imaging is done at Materials Engineering Department and Bioimaging Facility at the University of British Columbia by the author, under supervision of Mr. Jacob Kabel and Mr. Derrick Horne respectively.

In Chapter 3, both high speed visualization of creping mechanism and high speed imaging of tissue surface are done by author with help from Mr. Kui Pan, Ph.D. candidate from the same lab as the author.

In Chapter 4, tensile characterization of tissue materials are done by author with help from Mr. Kui Pan and Mr. Charly Jeunot, a former summer intern. The microtensile tests with *in situ* SEM imaging are done by author under supervision of James Drummond. Both the tensile characterization and microtensile test experiments were done at FP Innovation, Vancouver.

Contents

List of tables

List of figures

Glossary

Apparent density The mass of tissue material occupying unit apparent volume. This volume includes volume of fibers, pores and voids.

Basis weight Areal density of a paper or fabric product, that is, its mass per unit of area.

Bulk Inverse of density of paper products.

Bulk softness A perception of easily crumpling a structure lacking firmness.

Caliper Measure of thickness of paper products.

Felt Woven belt of wool, cotton or synthetic fibres used to transport web of paper.

Formation The manner in which paper fibres are mixed in a sheet of paper. Physical distribution and orientation of fibres and other solid constituents in the structure of a sheet of paper that affects its appearance and other physical properties.

Forming fabric Finely woven fabric fitted at the wet end of the tissue machine to support and provide drainage for the pulp suspension as it becomes a paper web.

Hardwood Pulpwood from broad leafed dicotyledonous deciduous trees, such as aspen, maple etc.

Softwood Wood obtained from evergreen, cone bearing species of trees, such as pines, spruces, hemlocks, etc., which are characterized by having needles.

Stock Various pulps, dyes, additives and other chemicals blended together in liquid form for paper-making.

Stretch The amount of strain a paper sheet can undergo before breaking.

Wire mark The impression made on the bottom side of a paper web by the surface contour of fabric pattern.

Acknowledgements

First, I would like to thank my research supervisors: Dr. Anasavarapu Srikantha Phani and Dr. Sheldon Green for their time, patience, and faith in me. I cannot emphasize enough how much their guidance and advice oriented me to be a critical thinker, as a researcher should be. Srikanth's sincere attention to every step of my research and Sheldon's innovative ideas and perspectives are the stepping stones of this thesis.

I would like to thank Anna Karin, Ashleigh Ward, Daniel Ricard, Ho Fan, James Drummond, Jimmy Jong, Timothy Patterson, and Xuejun Zou for their support and for sharing valuable industrial knowledge and experience. Guidance, training, and assistance provided by Derrick (SEM specialiast, UBC Bioimaging Facility) and Jacob (Former Electron Microscopist, UBC Materials Engineering) are sincerely appreciated.

I am thankful to the members of my examination committee: Dr. Gary S. Schajer and Dr. Mauricio Ponga, for generously offering time to evaluate and constructively criticize my work.

My lab mates, Manav, Kui, Masoud, Reza and Aashish are the most sincere researchers I have come across. They create an academic yet enjoyable environment in my lab, which constantly motivates me to perform better. The mutual insightful discussions there are really a crucial part of my research experience.

My friends: Claire, Nirmalendu, Harsh, Somesh, Prashant, Miguel, Adriana, Patrick, Faisal, Aishwarya, Mike, Ankita, Saurav, Juuso, Sarah, Fagun, Ketaki, and Shahzaib are always with me, through thick and thin. Special thanks to my past, present and future roommates (read friends): Kristian, Mielle, Keith, Meredith, Seth, Marina and Moshe for supporting me and being the awesome roommates you always are.

Last, but not the least, my mother Rinku Das, father Bhabananda Das, and late grandmother Laxmi Das are always in my thoughts and have an important role in this achievement.

To my family.

Chapter 1

Introduction

Light-weight tissue-paper products like bathroom tissues, facial napkins and kitchen towels are an integral part of modern life. The apparent density of these products is generally below 300 kg/m^3 and the basis weight is less than 50 gram per square meter (gsm) [3]. For comparison, the grammage of regular copy paper is 80 gsm and can be as high as 300 gsm for card boards. Unlike printing and packaging paper materials, tissue papers need to be more soft, stretchy, tough and water-absorbent. These properties are achieved by a specialized manufacturing technique called creping. Creping increases bulk, stretch and toughness by damaging the paper sheet in a controlled fashion and by introducing a strong micro-structure, known as the creping structure [3, 4, 5, 6]. Combined with damaged fibers and network characteristics, the creping structure is believed to govern the mechanical properties and quality of tissue products. Therefore, a careful understanding of creping mechanics, related manufacturing parameters, and how creped paper structural properties affect tissue quality is important.

Recently Pan et. al. developed a one dimensional discrete particle model [7] to simulate creping. This model was able to explain the underlying physics, quantify post-creping micro-structure, and predict the stress-strain behaviour of creped tissue. The theoretical work is complemented with experiments in this thesis. The primary focus of the thesis is developing experimental techniques to visualize creping and to quantify creping structure. The tensile properties of commercial tissue are also determined from experiments and visualization techniques are developed to observe the network structure deformation with load to understand the mechanism of deformation and failure. Section 1.1 is a brief description of creping in context of tissue production. Section 1.2 is an overview of the physics of creping. Section 1.3 describes crepe structure quantification methods. Section 1.4 is a synopsis of theories describing the stress-strain behaviour of paper products. Finally, section 1.5 lists the objectives, and describes the structure, of this thesis.

1.1   Tissue Production and Creping

Tissue production is a complex process involving various techniques. A simple schematic of tissue manufacturing process with related process parameters is shown in Fig. 1.1. The entire process can be divided into four major sub-processes: forming, dewatering, creping, and finally reeling and converting (see Fig. 1.1 top). Tissue production usually starts from a headbox at the

forming section (see the triangular shaped feature towards the left hand side in Fig. 1.1). It contains a very dilute slurry of mechanically or chemically refined pulp fibers, also known as stock, at 0.15%-0.5% solid content. The composition of fibers (see parameter 1 in Fig. 1.1) in the stock is important; more short hardwood fibers (aspen, maple etc.) are preferable for softer products like facial tissues whereas, longer softwood fibers (pine, beech, spruce etc.) are required for stronger products e.g. kitchen towels. In the forming section, one or multiple layers of stock fibers (together known as pulp mat) is(are) deposited and dewatered in between a forming fabric and a dewatering felt (sometimes another forming fabric is used instead of a dewatering felt). The topography of the forming fabric imparts some initial structure (see parameter 2 in Fig. 1.1) to the pulp mat. The pulp mat is then transferred to a water absorbing felt in the dewatering section, where the solids content of the mat is increased to about 20%. A pressure nip presses this mat against a rotating cast iron cylinder at this point. The pressing action not only expels water from the mat, but also densifies the mat and strengthens the bonds between fibers (see parameter 3 in Fig. 1.1). Finally, the wet mat, which has a similar consistency to cooked lasagna noodles, is transferred to the surface of Yankee dryer (the big circular feature at the right side in Fig. 1.1).

The rotating (40-50 rotations per minute) yankee drum is precoated with a mixture of adhesive chemicals, release agents and modifiers sprayed from a nozzle (see under the Yankee dryer in 1.1). The coating spray intimately adheres the wet mat to the yankee drum and forms a protective layer of chemicals on the yankee surface (see parameter 5 in Fig. 1.1). The internally steam-heated yankee and drying hoods rapidly increase the solid content of the web to 95% by the time it reaches the other end of the drum (see parameter 4 in Fig. 1.1), at which location, a sharp doctor blade scrapes the dry web off the surface. The violent interaction between the sheet and blade, known as dry creping, damages the network of fibers, resulting in foreshortening of the sheet, improved stretch, bulk and softness with concomitant tensile degradation. The strength and uniformity of adhesion between yankee surface and web is extremely important for efficient creping [6]. If the adhesion is strong and even, fiber-fiber bonds will break when the paper web hits the blade, increasing bulk, softness and absorbency. Too strong adhesion may result in sheet break whereas, weak adhesion will result in sheet falling off the yankee cylinder before it hits the blade.

Once creped, the damaged, compressed web is reeled downstream for converting and embossing at a lower speed than the yankee surface speed (see parameter 6 in Fig. 1.1). The difference between yankee dryer surface speed and reel speed divided by yankee surface speed is known as the creping ratio (see parameter 7 in Fig. 1.1). Since reeling speed of tissue is lower compared to yankee surface speed, more material is packed in a given length after creping. This increases the overall bulk of the tissue. The creping ratio is generally held between 15%-20% where bulk increases with increasing creping ratio [4]. High bulk is correlated with greater bulk softness and water absorption capacity.

Forming → **Dewatering** → **Creping** → **Reeling and converting**

1. Headbox Stock Furnish
- *Hardwood for softness.*
- *Softwood for strength.*
- *Consistency & flow rate governs basis weight.*

2. Forming Fabric Structure
- *Controls web-formation and fiber orientation.*

3. Nip pressure
- *Increases base sheet density.*
- *Increases web strength & sheet-yankee adhesion.*

4. Yankee Temp. (~100°C)
- *Decreases base sheet moisture-content.*
- *Controls base-sheet stiffness and sheet-yankee adhesion before creping.*

5. Coating Spray Chemistry
- *Adheres semi-wet web onto yankee.*
- *Forms a protective layer of chemicals and fibers on yankee surface.*

Machine Direction (MD)

Drying Hood

Yankee Dryer
(Diameter ~ 6 m Speed ~ 1500 m/min)

SC: ~ 40%

SC: ~ 95%

Headbox SC: ~ 0.5%

Pressure nip SC: ~ 20%

Forming Fabric

Dewatering Felt

Support Fabric

Adhesive spray nozzle

Doctor blade

Reel

6. Yankee speed (V_{in} ~ 1500 – 2000 m/min)
- *Yankee surface speed controls sheet drying time and moisture content.*
- *Indirectly controls base-sheet stiffness and sheet-yankee adhesion before creping by changing drying time.*

7. Creping Ratio (~ 15% – 20%) $\dfrac{V_{in} - V_{out}}{V_{in}}$
- *Controls bulk.*

8. Doctor Blade Geometry
- *Creping angle controls creping force magnitude and direction.*
- *Blade wear decreases crepe count and tissue quality.*

9. Creped Tissue
- *Softer, tougher. More stretchy and water absorbent than uncreped paper.*

- **1 and 2 are inputs to creping.**
- **3-8 govern the creping process.**
- **9 is the desired output product.**

Figure 1.1: Schematic of tissue manufacturing process and impactful parameters (1-9)
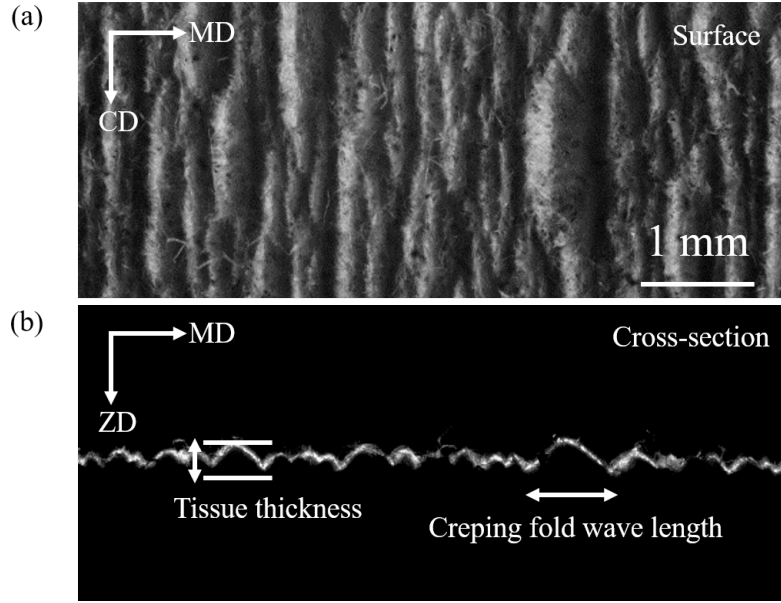
Figure 1.2: Creping structure as seen from a (a) surface image and a (b) cross-section image of a high basis weight creped tissue. The basis weight of the uncreped paper was 25 gsm and was creped in a crepe simulator. The surface image is taken under oblique diffuse light. The cross section is illuminated by a line laser and imaged subsequently. The creping folds can be seen clearly from both the surface and cross-section image. However the crepe folds are much smaller in a commercial tissue.

Observation of creped tissue surface reveals a series of folds, aligned roughly parallel to the cross direction (CD) (see Fig. 1.2 (a)). The folds are visible as approximately parallel bands of bright and dark regions. The actual micro-structure of these folds is seen clearly in a cross-section image (see Fig. 1.2 (b)). These folds are produced during creping and are key to increase machine direction (MD) stretch and bulk in the final tissue. Uniform and short crepe fold structure is usually, but not necessarily, desired in a good quality tissue. A multitude of factors e.g. forming fabric induced wire mark pattern (same as parameter 2 in Fig. 1.1), basis weight, web-yankee adhesion strength and creping blade geometry affect this fold structure length-scale and its distribution [8]. The distinct wire mark pattern generates finer crepe folds, which are generally in phase with the wire marks [4]. If the wire mark is too heavy, it creates holes in the sheet. High web basis weight and strong sheet-yankee adhesion generally creates finer crepe folds [5, 9].

A schematic of the geometry of creping blade is shown in Fig. 1.3. The angle between creping blade and yankee surface is known as creping angle. Creping angle also plays an important role by varying the creping force that doctor blade applies to scrape off the web from the yankee
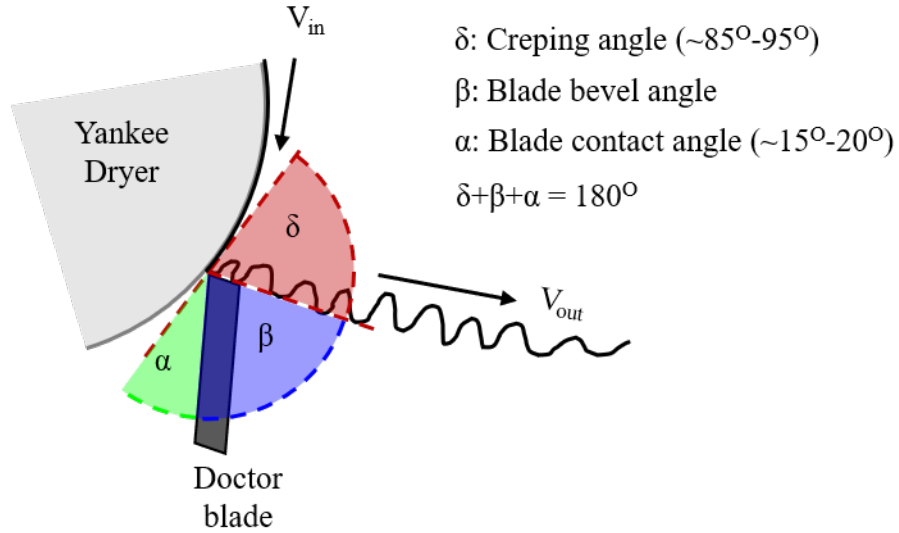
Figure 1.3: Simplified 2D schematic of doctor blade and Yankee dryer contact and various angles related to creping mechanism. The size of the doctor blade is exaggerated for clear presentation. In reality the blade size is much smaller compared to the size of the Yankee. The various angles shown are creping angle (δ), blade bevel angle (β), and blade contact angle (α). Nomenclature of the angles vary among industries and literature.

surface. In real tissue machines this angle is generally $85^o - 95^o$. An increase in creping angle generally creates a fine and uniform crepe structure [5]. Understandably, an optimal combination of these parameters is needed to produce a quality tissue. However, there is no systematic way of choosing values for these parameters because of the lack of scientific understanding of creping mechanism and the effect of the process parameters on the tissue quality. We will approach this problem with the objective to develop experimental techniques to understand creping mechanism, and to quantify tissue structural and mechanical properties. Data from these experiments will compliment analytical and numerical works.

1.2 Mechanism of Creping

Tissue production is extremely rapid. 30 meters of creped paper sheet containing hundreds of thousands of crepe folds can be manufactured each second. with each fold generation occurring within a few microseconds. High speed imaging studies close to the creping point and numerical simulations are two major approaches taken by previous researchers [5, 7, 9, 10, 11] to under-

Yankee Surface Adhesive Layer Web

V_{in}

Region of high stress concentration

Doctor Blade

Debonded web-segment

Plastic Deformation

Collapsed Fold

V_{out}

Thickness of web is much larger (50-60 times) than adhesive layer.

(a) Stress Development   (b) Crack Propagation   (c) Buckling   (d) Fold Formation
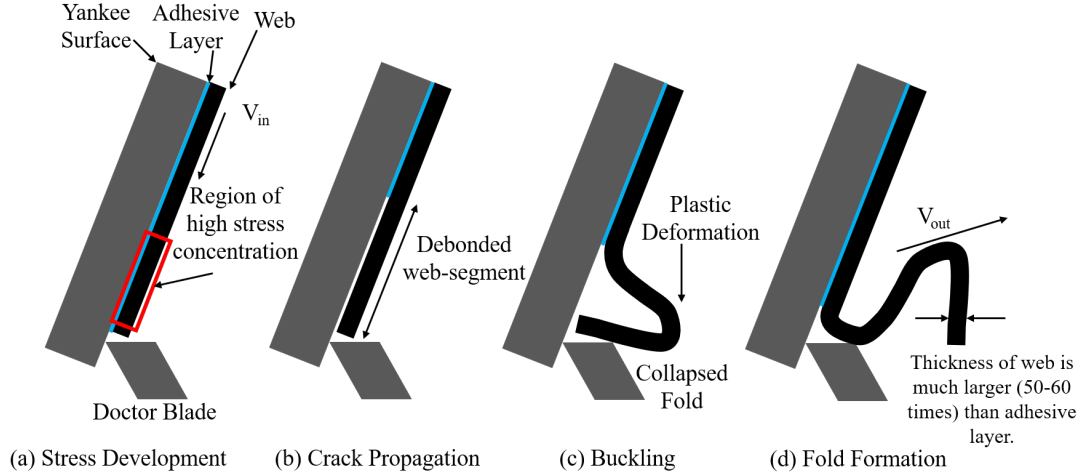
Figure 1.4: Four stages (a-d) of a creping fold formation. Only a cross-section of the tissue, blade and yankee is shown. The yankee drum surface is approximated as a linear surface. Wire mark patterns before creping and internal sheet damage are not shown in this schematic.

stand creping. High speed imaging in a real tissue machine, however, is notoriously difficult and expensive because of accessibility issues and the dusty, steamy environment. All published experimental studies are done either in small scale creping simulators or pilot tissue machines at significantly low production speed. In the last two decades, more emphasis has been placed on numerical simulation of creping based on the previous phenomenological observations. From these experimental and numerical studies, creping is understood as a fracture-driven buckle-delamination process.

Hollmark imaged the blade-sheet interaction during creping in a pilot tissue machine operating at 140 meters per minute and observed how the folds were generated [5]. Creping ratio in this experiment was held at 32%. According to this study, once the sheet hits the blade and gets separated from the surface, a loop forms at the edge of the blade. A second loop forms on top of the first one as more web is fed. This loop formation continues until the pile collapses and is pushed off from the yankee surface. This study gives a phenomenological description of the fold generation, but does not explain the underlying mechanics involved in this process. Rama-subramanium et al. built a laboratory scale creping device [9] and made similar observations at the blade-sheet interface. Typical yankee speed in their experiments was around 144 meters per minute but there was no creping ratio. They explained the mechanism of individual fold generation in four stages as shown in Fig. 1.4 (a) - (d). In the step (a), stress develops in the web and adhesive layer as the sheet hits the blade. This stress cracks the sheet-adhesive interface and the

6

crack propagates until the debonded segment reaches a critical length in step (b). Afterwards in step (c) and (d), the debonded segment of web buckles to produce a single fold and gets pushed outwards. This process repeats itself to give the continuously folded structure that is similar to what is observed in commercial tissues.

A significant drawback of all the experimental works was that the yankee surface-speed was an order of magnitude lower compared to a real tissue machine. Yankee speed is an important parameter because it controls the drying time of partially wet web on the yankee surface. Variation in drying time can alter moisture content and elastic properties of both web and adhesive layer as well as sheet yankee adhesion just before creping. Also the effect of inertia of web on creping force is not known. The mechanism of crepe at high speed has not been explored extensively and whether it is significantly different or not is still an open question. This literature-gap will be partially addressed in this thesis.

Ramasubramanium et. al developed a mechanics of material model of creping [10] based on strength based failure criterion of the adhesive layer and Euler buckling analysis of the paper sheet. This model predicted results qualitatively consistent with experimental data and known industrial observations. However it was a quasi static analysis and did not try to predict the mechanism at higher speeds. More recently, Pan et. al. applied a discrete element model [7] to simulate creping of a single layer of elastic web bonded to a rigid yankee surface at realistic yankee surface speed. They observed similar stress development, delamination and buckling phenomenon in the numerical simulation of creping fold formation. Creping angle and web thickness before creping were shown to be most significant factors affecting creping fold wavelength and the effect of yankee speed was shown to be negligible. But it is important to point out that in the model, the effect of changing yankee speed on properties of the sheet and adhesive layer was not taken into account. Hence the conclusion about effect of creping speed is likely not to be realistic. Also, this model was limited by the one dimensional simplification of paper, its homogeneity and elastic response.

It is evident from the previous works that creping significantly alters the the planar fiber-network structure of uncreped paper. It plastically bends individual fibers, introduces fiber axial micro-compression, and causes internal fiber-fiber bond damage [3]. High bulk, stretch, softness, water absorption capability of tissue comes from this altered structure. Therefore, an understanding of tissue micro-structure and related quantifiable parameters is important to evaluate creping-efficiency and tissue-quality. This is discussed in the next section.

1.3   Crepe Structure Quantification

Creped tissue paper is primarily a network of plastically deformed loosely bonded fibers, preferably aligned with the machine direction, with a folding pattern. The in plane and out of plane dimensions of this folding pattern varies in both machine and cross direction as a result of variation in formation, sheet yankee-adhesion and many other factors. Although the wave-like pat-

terns are not exactly periodic, two quantifiable structural parameters can be attributed to them. First, the number of folds per unit machine direction length of unstretched tissue paper is known as the **crepe count**. There is no direct correlation between tissue quality and crepe count, but uniform small crepes are generally an indication of stable production and high-quality product. Nonuniform and bigger folds indicate non uniform or inadequate adhesion between sheet and yankee surface, poor formation or excessive blade wear. So, crepe count is often determined in a tissue machine during production (online) or in laboratory (offline) after creping to assess tissue quality and predict the time of blade change. Out of plane dimension of the crepe folds is known as **creping amplitude**, which increases tissue caliper and bulk. This section is devoted to explaining the techniques available to quantify the structural aspects of crepe folds, namely crepe count and creping amplitude.

There is no standard protocol for crepe count measurement, partially because it is not a well-defined parameter in tissue industry. Generally creped tissue surface is imaged in laboratory at 60X–70X magnification to identify peaks and valleys. Distance between consecutive peaks or valleys is measured to find fold wavelength and reciprocal of the measurement is recorded as crepe frequency [12]. Alternatively, a 3D image of tissue surface structure can be reconstructed by confocal microscopy. Cross-sections along machine direction can be extracted from the 3D structure to determine crepe count. In another technique, a mechanical profilometer can be used to measure surface profile of tissue and dominant frequency can be extracted using Fourier Transformation. The dominant frequency is believed to come from crepe folds and used as a measure of crepe count [12]. Recently, photometric stereo method based surface profile characterization has also been used instead of profilometer [13]. Microtome sectioning of tissue cross-section can be done to take images of cross-section along machine direction. These images can be analyzed to extract crepe frequency as well as out of plane amplitude of crepe folds [14]. All these laboratory based offline methods are time consuming and a large number of measurements are required for a statistically meaningful measurement. These techniques are hard to implement in a tissue-machine to measure crepe count or caliper in real time during production.

Sabater et. al. demonstrated a way to measure the tissue surface state index or undulatory variations of tissue surface just after creping in a running tissue machine [15]. In this method, a laser light is directed on the moving creped surface and a photoelectric device is placed at an angle to collect the back-scattered laser light. Using optical proximity detection method and suitable signal analysis, geometric data of the creped sheet along a straight line in machine direction can be extracted. This method can be employed online to continuously measure crepe fold pitch and the average amplitude of the crepe folds. But this method does not give information on cross directional variability of crepe count since it measures crepe pitch along machine direction in a straight line.

In the past few years, measurement of crepe structure using surface images has been investigated because of its simplicity and potential of online measurement across the paper web [16, 17] In this method, bright light is shined from an oblique angle relative to the plane of

the paper, preferably along machine direction. Hills in the crepe structure are perceived as bright regions and the valleys as darker regions. However, the grey-scale periodicity seen in surface images is a perception of the folds and is not related to actual physical depth. Images are processed using suitable signal processing methods e.g. spectral analysis to extract dominant frequency of the folds. Further analysis has also been done to quantify small scale surface roughness [18]. Recently due to a drop in the price of high-speed imaging equipment and an increase in computational power, these techniques are incorporated in online tissue quality control systems [18]. However, the spatial pixel resolution of surface images are about 60-100 μm. For commercial grade fine tissue papers, crepe folds can be as small as 200 μm. A better resolution imaging system can improve quality of measurements significantly. In Chapter 2 of this thesis, development and application of a surface imaging-based crepe-count measurement technique are discussed. A high resolution commercial camera and a diffuse light source is used to build a laboratory scale crepe-count device first. Image pixel resolution is about 7 μm. Instead of computing crepe-count as a single number to characterize tissues, emphasis is given on determining the distribution of crepe-counts. Distribution or variability in crepe count measurement from a surface image can tell us about the uniformity of creping, a highly desired characteristic of good quality tissue. To prove reliability of the surface image based crepe count measurement technique, Scanning Electron Microscope images of tissue cross-sections are analyzed to determine crepe-count and compared against surface imaging measurements. Good correlation is found. In chapter 3, the surface image based quantification method is used in a real tissue machine to extract crepe count of tissue online. Images of tissue sheet moving at 25 m/min are taken using a high speed flash (pulse width 1 μs) synchronized with a commercial camera and quantified online. The measurements are compared with offline crepe counts. Again good correlation was found between the measurements. Capability of the surface imaging system as a online process monitoring tool is established. If this system is integrated with a tissue machine, systematic studies on effects of blade wear, furnish, forming fabric, and adhesive coating can be done to complement theoretical studies and numerical simulations of creping.

1.4 Tensile Properties of Paper

Tensile behaviour of paper materials change significantly after creping. Fig. 1.5 shows typical stress strain curves for paper before and after creping [4]. Evidently creping increases stretch and work to rupture with a corresponding degradation in strength and elastic modulus, especially in machine direction (MD). The entire stress strain curve in both machine and cross direction for tissue and low-density grades is important for several reasons. The strength characteristics along machine direction directly influences runnability [3]. Cross direction stretch is important for successful converting operations and embossing. Elastic modulus of dry creped tissue is widely believed to govern bulk softness. Recently attempts have been made to produce soft tissue paper without creping, but those attempts have not been particularly successful. Therefore, an
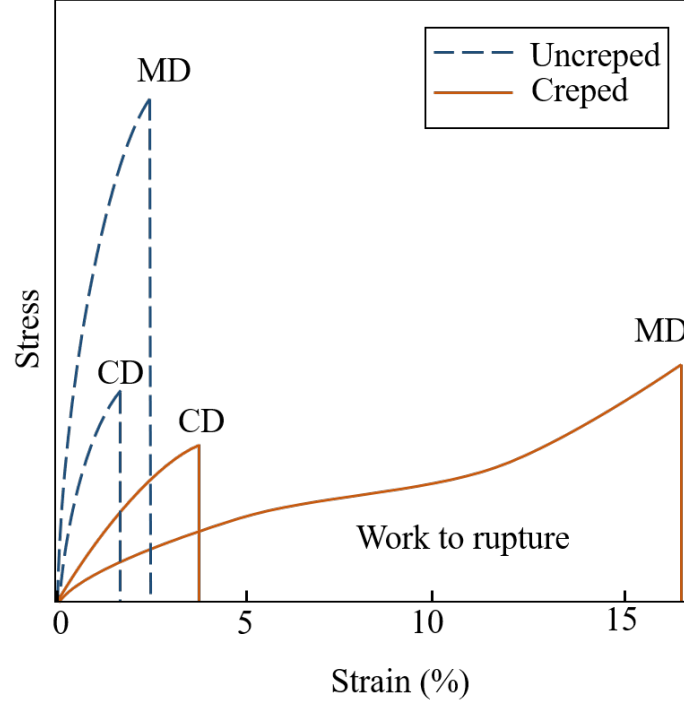
Figure 1.5: Stress strain behaviour of paper before and after creping. Creping increases stretch and work to rupture and lowers strength in both machine direction (MD) and cross direction (CD). However, the impact is higher along MD. Reconstructed from [4]

understanding of the principal mechanisms that govern the tensile response, elastic modulus, strength and stretch is important to successfully design a tissue as per consumer-requirement with efficient production speed.

Tensile response of paper materials, creped or uncreped, have significant nonlinearity. In past half a century, two-dimensional network theories [19, 20, 21] have been developed to partially explain tensile behaviour of uncreped paper materials. Not much has been done to understand the tensile behaviour of creped tissues. Cox's analytical expression of elastic modulus of a plane fibrous network is the foundation of network theory for paper [19]. He models the fiber network as a homogeneous mat of systematically oriented infinitely long, straight, linearly elastic fibers. He assumes perfect inter-fiber bonding free of friction and sliding and considers only axial stiffness of the fibers in his analysis. Assuming an initial homogeneous stress field, he derives an analytical expression of elastic modulus of the network and concludes that under the assumption of randomly oriented fibers, elastic modulus of the network is one-third

of elastic modulus of fiber. This conclusion is experimentally verified for high density paper materials [20] made of straight fibers free from any gross kinks and cramps. These fibers have a linear tensile response. High density or intimate fiber fiber bonding is important to create a near-homogeneous stress field. However in reality, elastic modulus of paper materials is less than one third of average elastic modulus of fibers. This is because of two reasons. First, most pulp fibers used for paper and tissue production have a lower elastic modulus after pulping because of the nature of pulping process and the fibers are often oriented preferentially than randomly in the sheet. Second, for low density paper products, stress distribution through fiber length can vary giving rise to inhomogeneous stress field and inefficient inter fiber stress transfer. These factors are not taken care of in Cox's theory. Also, Cox's analytical model does not give insight into the viscoelastic nature of paper materials and cannot be extended to plastic regime of the tensile response.

Page et. al. modified the analytical expression of elastic modulus derived by Cox. Based on experimental observations they concluded that entire tensile response of fibers, degree of inter-fiber bonding and presence of kink, curl and micro compression in fibers affect elastic modulus of paper [20, 21, 22]. Three factors were incorporated in the expression of elastic modulus. The first depends on average fiber elastic modulus. The second one takes into account distribution of fiber orientation and the third one depends on fiber-fiber bond density or relative bonded area. The same argument of three governing factors was extended to plastic region of the tensile response. Non-linearity of the stress strain curves was believed to be largely related to the non-linear tensile response of fibers [23, 24]. Another theory behind the strain-softening behaviour and plasticity of paper is based on the concept of progressive micro-damage and rupture of fiber-fiber bonds with load from the very beginning of straining process [25]. However the second view, also known as a structuralist view, is largely discredited by experimental evidence [23].

However, in both Cox's work and Page's modified theory, the underlying assumption of a planar mat of straight fibers does not hold true for creped tissue papers. Creped tissue, as described before, consists of loosely bonded fibers that are deformed plastically out of plane. So, the applicability of the analytical theory developed by Cox and modified network theories built upon it is questionable for creped tissue. Also tissue paper network structure can undergo significant deformation to accommodate large strain before failure, which changes the fiber orientation factor of elastic modulus. Because of the complex nature of creped tissue paper, no theoretical work has been done to understand the entire stress-strain behaviour. Observation of structural evolution of tissue papers is a starting point to understand how the structure responds mechanically to load. In Chapter 4 of this thesis, imaging techniques are used to observe deformation of tissue fiber network at various levels of strain to delineate the underlying network behaviour.

1.5   Objectives and Outline

Based on the above literature review and the gaps found in understanding creping mechanism and mechanical properties of creped tissue, the following objectives have been identified for this thesis.

1. To develop and validate a surface image based visualization technique and processing algorithm to quantify crepe structure of tissue paper.

2. To demonstrate the capability of high speed imaging techniques for imaging and quantifying tissue structure in a running machine.

3. To visualize creping mechanism at high speed regime ($>$1000 m/min).

4. To characterize tensile response of crepe tissue with simultaneous observation of the network deformation.

In Chapter 2, a surface image based crepe count measurement technique is developed and validated using measurements from through thickness cross-sectional images of tissue. In Chapter 3, it is demonstrated that the surface imaging technique can be integrated with a high-speed imaging setup to do online crepe count measurement. Also a line laser based cross-section imaging technique integrated with a high speed camera is used to observe creping mechanism at high speed. In Chapter 4, structural evolution of tissue network under tensile load along machine direction is explained. Finally conclusion and future works are presented in Chapter 5.

Chapter 2

Tissue Structure Quantification

2.1 Introduction

Experimental techniques to visualize and quantify creped tissue structure have been explored before [14, 15, 16]. These techniques can be broadly classified in four different types: cross section imaging, surface imaging, reconstruction of line profile, and reconstruction of surface profiles of tissues (see Section 1.3 for more details). A brief comparison of these techniques is given below in Table 2.1.

Table 2.1: Comparison of crepe structure quantification methods

Type	Technique	Measurable quantity	Advantage	Disadvantage
Cross-section imaging	• Microtome sectioning and imaging	• Crepe count • Crepe fold amplitude	• Accurate	• Time consuming • Extremely variable • No online application
Surface imaging	• Stereo microscopy • High resolution surface imaging with oblique light source	• Crepe count • Caliper • Free fiber ends	• Fast and robust • Online application	• No out of plane creping amplitude information. • Large data requirement for caliper estimation • Accuracy not investigated
Line profile reconstruction along machine direction	• Laser based optical proximity detection	• Crepe count • Crepe fold amplitude	• Fast and accurate • Online application	• No cross-direction information in online environment
Surface profile reconstruction	• Profilometry • Confocal microscopy • Photometric stereo	• Crepe count • Surface roughness • Free fiber ends	• Robust and accurate	• Time consuming • No online application

Cross section imaging and surface profile reconstruction [14] can accurately quantify both crepe count and creping amplitude. However, data acquisition in these techniques is time con-

suming, making it difficult to implement them in a running tissue machine. Line profile reconstruction method based on laser based optical proximity detection is faster and can be integrated in a running tissue machine [15]. Recently, the surface imaging technique has been used in a tissue machine to extract crepe count and caliper in real time [18]. However, the accuracy of the crepe count measurement based on surface images has not been investigated before. In this chapter, tissue structure quantification technique based on cross section imaging (**through-thickness**) of tissue paper is described first (section 2.2) followed by a surface imaging based technique (section 2.3). The results are then compared in section 2.4 to investigate the accuracy and robustness of surface imaging methods in determining **crepe count and its distribution**. A systematic protocol of imaging and analysis is also established from this exercise.

To image cross sections, a line laser and a Scanning Electron Microscope (SEM) is used. The line laser based illumination technique (combined with a commercial DSLR camera) to image tissue cross section is very useful because of its minimal invasion on crepe structure. This technique works well for tissues with high basis weight (>25 gsm per ply) and with coarse crepe structure (>500 μm creping wavelength). However for low basis weight commercial tissues with finer crepes, this technique is seen to have inadequate image resolution. For these tissues, SEM is used. SEM has very high image resolution and depth of focus, which ensures clear images required for finer crepe structure. Suitable **image analysis** methods are used to extract the creping pattern from the images. Finally quantification techniques are developed to quantify the crepe count. An experimental setup is then built to image tissue surface. An image processing and quantification algorithm is developed to extract dominant crepe count. Though the imaging concept is same as any other offline surface-imaging method, this technique can quantify crepe count with an estimation of its variability in a tissue. Degree of variability in crepe count is important to tissue manufacturers for quality control purpose.

Two high basis weight tissue paper samples produced in a crepe simulator and four low basis weight commercial grade tissues are characterized in this experiment. These samples, named Grade 1-6 were collected immediately after creping without any embossing or converting. Grade 1 and Grade 2 are high basis weight samples. Single ply laboratory made paper strips were creped in a crepe simulator (see section 3.1.1 for more details) and collected. Basis weight of the uncreped sheet was 25 gsm and caliper was 63.923 μm. Grades 3-6 are low basis weight commercial tissues produced in a real tissue machine. Details of the Grade 3-6 is in Table 2.3.

Table 2.2: Details of Grade 3-6. All the measurements were done on a 2 ply creped tissue

Name	Basis Weight (gsm)	Caliper (μm)	Softness (Handfeel)	Nature of end use
Grade 3	14.3	100	78	bathroom tissue
Grade 4	20.1	158	80	bathroom tissue
Grade 5	16.9	116	90	facial tissue
Grade 6	17.9	151	85	bathroom tissue

2.2 Through-thickness Quantification

Imaging of tissue cross section is challenging because tissue paper is very thin and delicate. Very high image resolution and a sample preparation technique with minimal effect on tissue structure are imperative to get an image that can clearly represent the undeformed micro-structure. Two different ways of visualizing tissue cross section, namely line laser and SEM, are explored in this section. Suitable image processing and analysis methods are used to extract and quantify the creping structure.

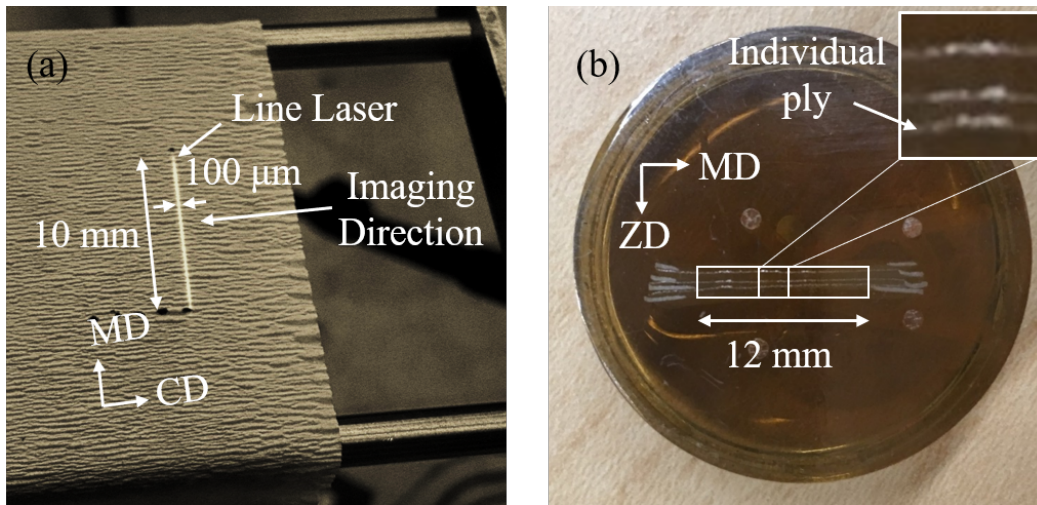### 2.2.1 Cross section Imaging Methods

Figure 2.1: Tissue cross section imaging techniques based on (a) Line laser illumination and (b) Scanning Electron Microscope (SEM) imaging

Fig. 2.1 (a) illustrates the line laser based illumination technique used to image tissue cross section. A low power (500 mW) line laser is used to illuminate a narrow cross section (see figure) along the machine direction. The illuminated cross section is imaged subsequently using a high-resolution commercial camera (not shown) placed at an angle to the tissue surface. The direction of imaging is shown in the figure. This method was successful in imaging high basis weight grades (Grades 1-2) with high caliper, less porosity and large crepe fold size. To reiterate, these were not commercial grade tissues, but rather produced in a laboratory scale creping rig.

Caliper and the dominant length-scale of crepe folds are significantly smaller for low basis weight commercial grade bathroom and facial tissues. So, the image resolution in line-laser based imaging is not enough to capture the micro structure adequately. Low magnification Scanning Electron Microscope imaging is used for these low-density commercial grade tissues

(Grades 3-6). However, SEM imaging is not as straightforward and non-invasive as the previously discussed line laser imaging, but rather involves a complex sample preparation technique [26]. One very common technique is to impregnate delicate samples in a suitable resin block. For tissues, anhydrous Spurrs Resin is used to completely fossilize multiple rectangular strips of tissue paper in a cylindrical plastic mold. For two-ply tissues, each ply is separated before putting them in the mold. Bleached cardboard strips are placed between two consecutive plies to prevent them from sticking together. The card boards strips also hold the samples in place during the baking of the resin block at 70° C. After 24 hours the cylindrical resin block is taken out of the oven and separated from the mold. Fig. 2.1 (b) shows one side of such a resin block with 3 fossilized tissue plies. These layers are visible as very thin white horizontal lines (shown in inset) in the middle of the block. The short thick white lines close to the edges are parts of cardboard strips that were used to hold the tissue samples in place. The entire surface is polished and chemically etched to reveal several microns of unconstrained tissue structure. A very thin ($\sim$5 nm) conductive layer of gold palladium coating is deposited on the entire surface and imaged with a Scanning Electron Microscope at 100X magnification.

2.2.2   Analysis

Typical cross section images based on line laser illumination and SEM are shown in Fig. 2.2 (a) and (b) respectively. The magnification is much higher in the SEM image compared to the line laser technique. This makes the SEM images much detailed compared to those obtained from line laser. This can be appreciated from the level of details that can be seen in SEM images (see Fig. 2.4 top). Image details of a typical line laser and an SEM image are given below.

Table 2.3: Details of an image obtained from line laser and from SEM technique

Name	Spatial dimension (mm $\times$ mm)	Spatial resolution (μm / pixel)	Cross section length along MD (mm)
Line laser	10×4.67	25.39	10
SEM	1.28×0.59	1	1.28

The superimposed blue lines on the cross section images approximately follow the creping fold structure. Image analysis methods are used to extract these patterns. For images taken with line laser illumination (Fig. 2.2 (a)), greyscale-intensity weighted average distance of the pixels from the bottom edge is used as a measure to represent the creping pattern. In Scanning Electron Microscope images, top and bottom peripheral lines (black lines in Fig. 2.2 (b)) of the cross section are extracted first using edge detection. The mid line of top and bottom peripheral lines is then extracted to represent the creping pattern. The creping patterns are smoothed using a third order Savitzky Golay filter.

Clearly, the observed creping structures are not exactly periodic. Wavelength and amplitude of the folds vary as we go along machine direction. However, dominant wavelength and fre-
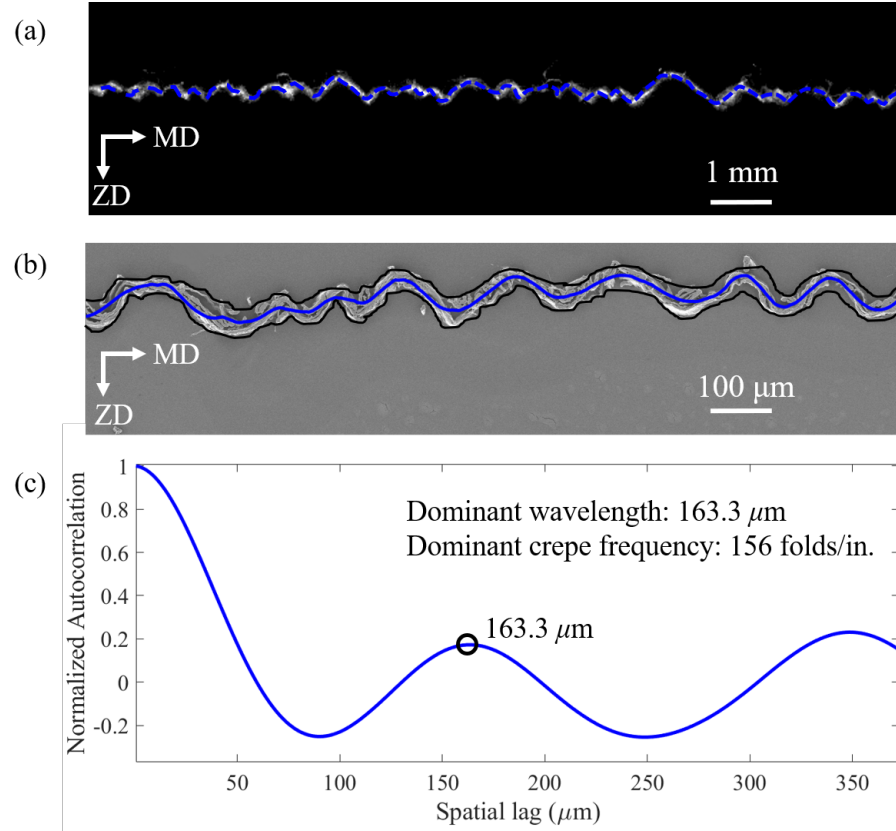
Figure 2.2: Typical tissue cross section images and analysis methodology. Images obtained from Line laser imaging (a) and SEM imaging (b) with extracted creping patterns (in blue). The dominant creping frequency of the creping fold pattern shown in (b) is obtained from its autocorrelation function in (c).

quency of these folds can be extracted from their autocorrelation function. The advantage of using autocorrelation function over popular Fourier Transformation or power spectral density is its versatility in determining dominant periodicity for any kind of signals, harmonic or non-harmonic. Also this technique is less sensitive to image noises, adaptable to any signal length, and computationally more efficient.

Part of the autocorrelation function of the extracted cross section shown in Fig. 2.2 (b) is given in Fig. 2.2 (c). The inherent periodicity of the cross section is well represented by the periodic nature of the autocorrelation function. Position of the first peak (indicated by a black circle in figure) is used as a measure of dominant fold wavelength of the cross section. Its inverse is used as a measure of dominant crepe frequency of the cross section. For each grade of tissue, several cross section images are taken and analyzed for a statistically robust estimation of crepe count. Each image is taken at a different location (several meters apart) of the tissue for

independent and unbiased sample images. Therefore dominant frequency of each cross section is independent from the others. The mean of dominant crepe frequencies of all the cross sections is calculated to estimate the dominant crepe count of one grade. Sample standard deviation of the dominant creping frequencies is used as a measure of variation in crepe count. Results are presented in next section.

2.2.3 Result

Grades 1-6 are characterized using the cross section quantification technique. Dominant mean creping wavelengths and crepe counts are tabulated in Table 2.4. The number of images analyzed (sample size, n) are given in the second column. Dominant creping wavelength and crepe count for all the grades are given in third and fourth column respectively. It can be readily seen that Grade 1 and 2 have much lower dominant crepe count, therefore larger creping wavelengths, compared to Grades 3-6. This is expected since the commercial grade tissues (Grades 3-6) are much finely creped than the samples produced in the crepe simulator. Among grades 3-6, grades 3 and 5 have similar dominant crepe count, which is significantly higher than grades 4 and 6. This indicates that there is a difference in length scale of crepe folds among the commercial grades as well. This difference can be visually observed from the cross section images (discussed later). There is also a large variation associated with each crepe count measurement. This is evident from the standard deviation values, which means that the creping fold structure of a tissue grade varies spatially. The source of this variation is the stochastic nature of creping process, inhomogeneity in the base sheet and sheet yankee adhesion, which in turn affect the creping pattern. This variation is not associated with the accuracy of measurement, but an indication of randomness of the crepe structure in tissue.

The summarized results for all six grades are explored in Fig. 2.3 - 2.5 in more detail, visually and statistically. For clear presentation, 2 grades are grouped together in one figure. For both grades, typical cross section images are shown at top. In each image, "MD" represents machine direction and "ZD" represents thickness direction. From Fig. 2.3, it can be seen that

Table 2.4: Mean dominant wavelengths and crepe counts of Grades 1-6 based on through thickness imaging.

Name	Number of images , n	Mean dominant wavelength (μm)	Mean dominant crepe count (folds/in.)
Grade 1	71	671 ± 143	40 ± 11
Grade 2	44	583 ± 145	47 ± 12
Grade 3	22	246 ± 60	109 ± 27
Grade 4	16	321 ± 68	82 ± 17
Grade 5	18	252 ± 61	106 ± 25
Grade 6	17	342 ± 61	77 ± 14

Figure 2.3: Typical cross section images (top) obtained from line laser based imaging and corresponding histograms (bottom) of crepe count for Grade 1 and Grade 2. Mean (μ), sample standard deviation (σ) of crepe counts, and sample size (n) are indicated in each histogram. Y axes of the histograms have been normalized with respect to sample size (n).)
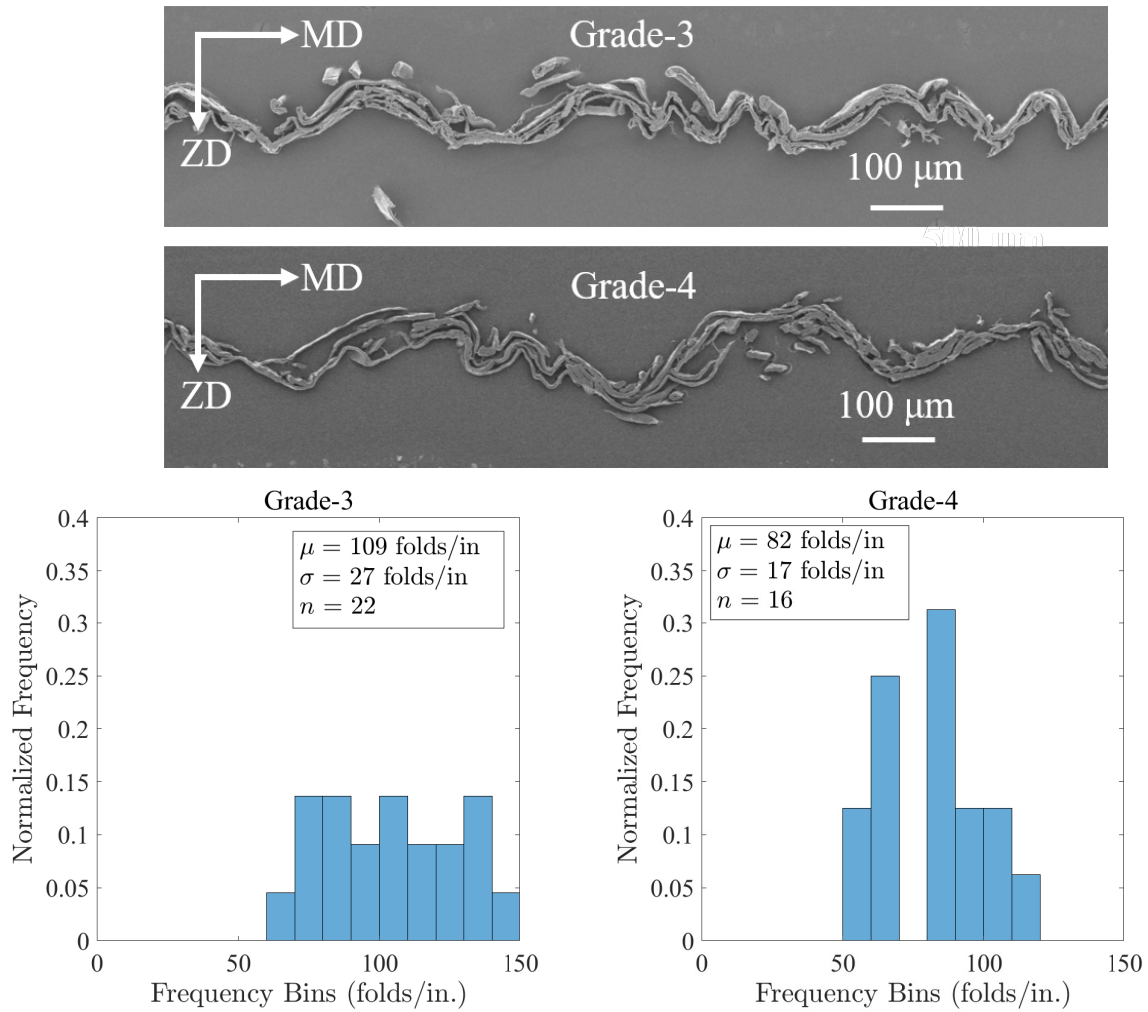
Figure 2.4: Typical cross section images (top) obtained from SEM imaging and corresponding histograms (bottom) of crepe count for Grade 3 and Grade 4. Mean (μ), sample standard deviation (σ) of crepe counts, and sample size (n) are indicated in each histogram. Y axes of the histograms have been normalized with respect to sample size (n).)
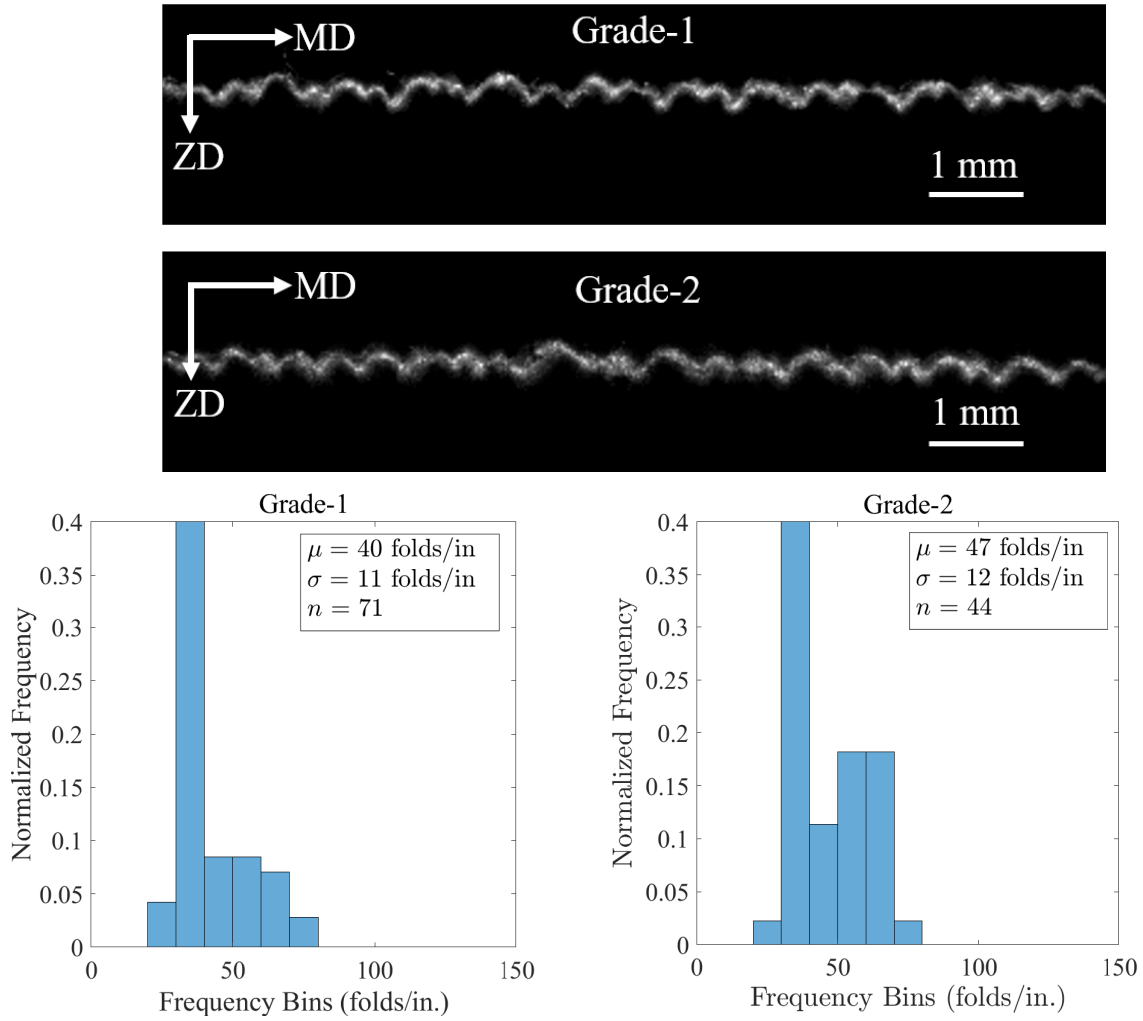
Figure 2.5: Typical cross section images (top) obtained from SEM imaging and corresponding histograms (bottom) of crepe count for Grade 5 and Grade 6. Mean (μ), sample standard deviation (σ) of crepe counts, and sample size (n) are indicated in each histogram. Y axes of the histograms have been normalized with respect to sample size (n).)
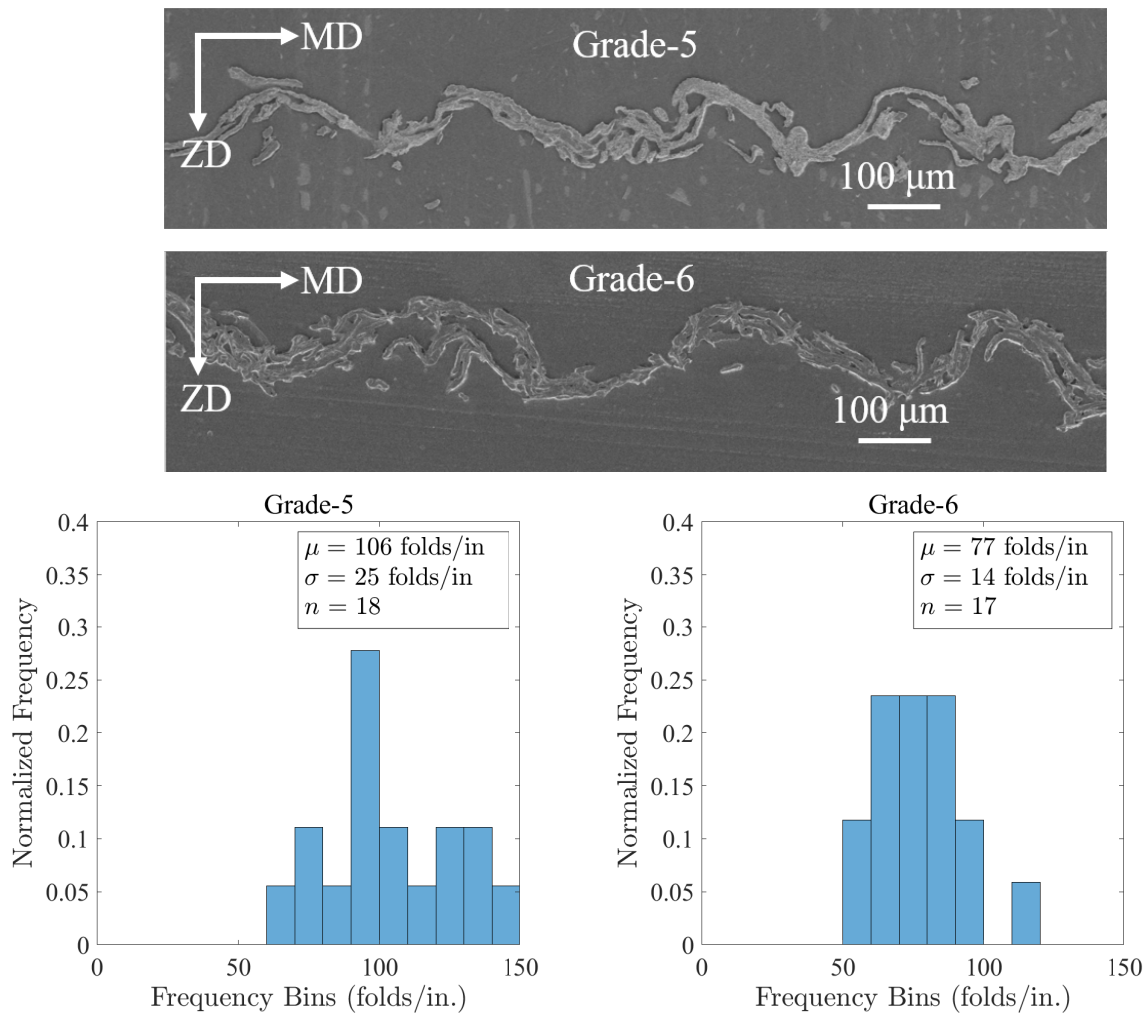
21

the wavelength of crepe folds in Grade 1 and 2 is approximately half a mm (compare with the scale bar). This is in alignment with the mean dominant wavelength found for these 2 grades (see Table 2.4, column 3). For grades 3-6 the creping folds are smaller than grade 1 and 2 (see SEM images in Fig. 2.4 and 2.5 and compare with scale bar). It can also be seen that grade 3 and 5 have smaller folds compared to grade 4 and 6, which is again consistent with the previous discussion of dominant creping wavelengths and crepe counts.

The histograms of dominant crepe frequencies are shown below the cross section images in each figure. The non-periodic nature of the folds and spatial variation are evident here from the wide distribution of the creping frequencies in the histograms. However, the number of sampled cross sections is statistically insignificant (except for Grade 1 and 2) to draw conclusions about the nature of distribution of these dominant crepe frequencies. To get a more statistically robust value of mean crepe count and a better understanding of the distribution, more cross section images need to be analyzed. However, the large amount of effort needed to take cross section images limits the number of images that can be taken. This problem can be alleviated by analyzing surface images. This will be discussed in the next section. To conclude, in spite of the limited number of samples, the cross section imaging can differentiate between tissue grades with significantly different crepe counts, both visually and quantitatively.

2.3   Surface Image Quantification

Surface image based quantification of crepe structure for Grade 1-6 is carried out to estimate crepe count and then compared with the results obtained using the through thickness technique. The goal is to demonstrate the capability of the surface imaging technique as a potentially more powerful tool to accurately estimate mean crepe count and the distribution.

2.3.1   Surface Imaging Setup

The tissue surface imaging setup is shown in Fig. 2.6. The setup consists of a tensile stage with two grips that hold a tissue sample under suitable tension, a diffuse light source (VELA one flash), a highly uniform back-light source (SCHOTT A08925 and A20500 ACE 1 EKE lamp) and a DSLR camera (Nikon D7000) placed perpendicular to the tissue surface. Tissue samples of 100 mm length along machine direction and 25.4 mm width along cross direction are cut and placed between the jaws in the imaging area. The tissue holder grip on left hand side is fixed. The other grip can be linearly displaced along the stage. It is attached to a pulley and weight system (not shown in figure) for tension loading. It is important to apply a low tensile load (< 5 N/m) along machine direction to avoid wrinkling and deflection of tissue surface under its own weight while imaging. The wrinkles and deflection of surface stands in the way of uniform illumination, which is imperative for a good quality surface image. The diffuse light used to illuminate the tissue surface is tilted at an angle θ to the normal of tissue surface
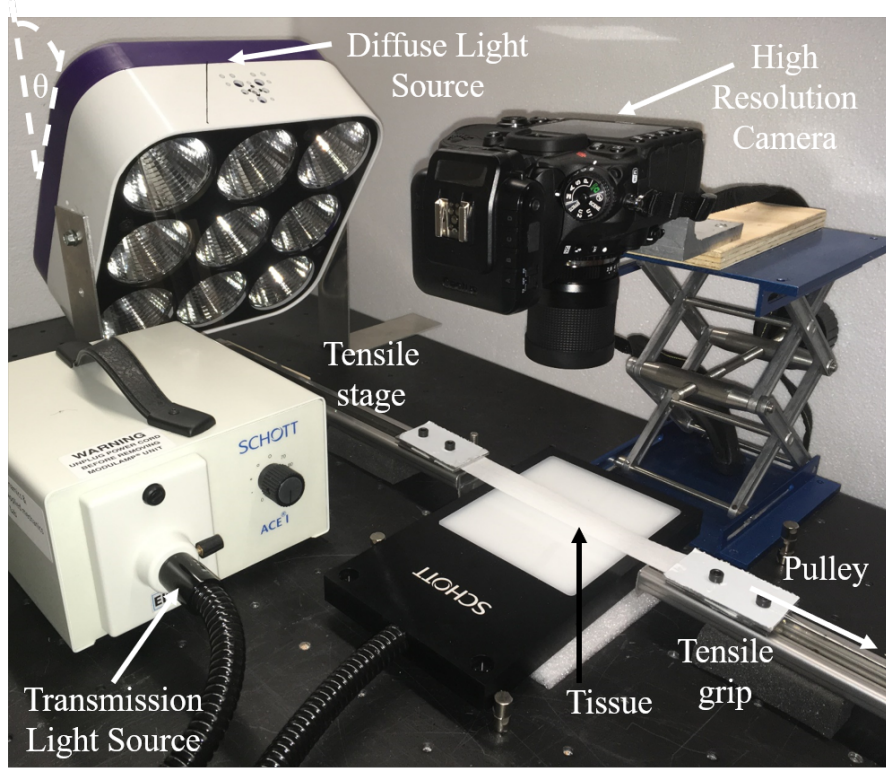
Figure 2.6: Tissue surface imaging setup

to highlight the crepe folds which are not clearly visible under ambient light. This angle is generally held between 50 to 70 degrees. It is seen that varying this angle does not produce significant differences in measurement. In a different imaging configuration, the uniform back-light can be placed below the sample to expose the internal network structure.

2.3.2 Analysis

Analysis methodology to extract mean dominant crepe count and corresponding variability from surface images is shown in Fig. 2.7. A typical surface image of a commercial tissue (Grade-6) is shown in Fig. 2.7 (a). The crepe structures are visible as alternate bands of bright and dark regions aligned roughly with cross direction. There are some very large scale intensity variation in some areas of the image. This comes from large scale physical undulation in surface. They are not related to creping structure. Dimensions of the image along machine and cross direction are denoted as l_{im}^{MD} and l_{im}^{CD} respectively. The thin rectangular box in the image indicates a typical cross section along machine direction. Length of this cross section (l_{cs}^{MD}) along machine
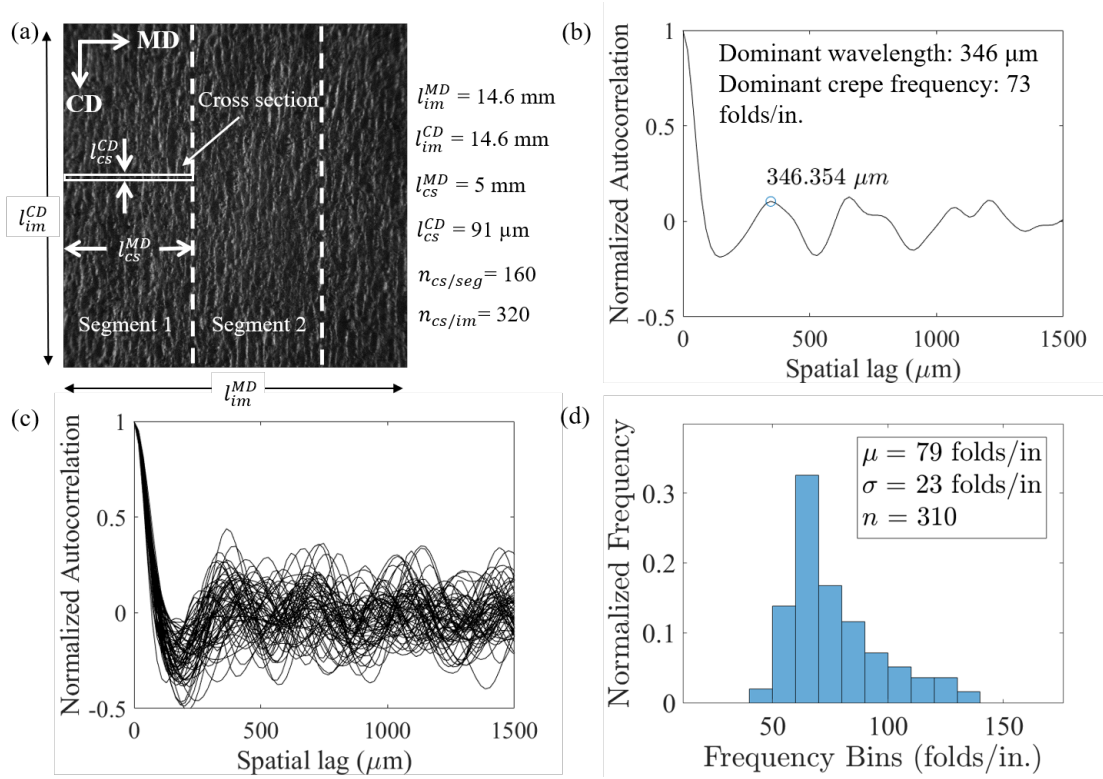
Figure 2.7: Analysis methodology to extract mean dominant crepe count from one surface image. Typical surface image (a) of a commercial tissue. The image has 2 segments. 160 cross sections can be extracted from each segment. A typical cross section (white rectangle) is shown in segment 1. Autocorrelation function of the cross section is shown in (b). Cloud of autocorrelation functions of multiple cross sections in segment 1 is shown in (c) and histogram of crepe frequencies of all the cross section in the image is shown in (d). Note that sample size of the histogram (n=310) is less than $n_{cs/im}$=320. 10 cross sections were ignored as the dominant crepe frequencies found from them were statistical outliers.

direction is taken as 5 mm. There are typically at least 10 or more crepe folds in this length for a commercial grade tissue. However, this length may be changed for other grades, depending on the coarseness of crepe structure. Tissues will coarser crepe folds may need a larger cross section length to adequately represent the crepe structure. A typical cross section width should be an order of magnitude smaller than the cross direction width of crepe folds. Typically, width of crepe folds are in the length scale of mm. Therefore, one typical cross section width (l_{cs}^{CD}) can be around 100 μm or less. Multiple rows of pixels are averaged spatially along cross-direction over the width to extract one cross section. The spatial averaging also reduces noise in greyscale intensity of the image.

Since the image in Fig. 2.7 (a) is much longer in machine direction than the length of

cross section, it can be segmented in at least 2 parts in machine direction. Number of segments ($n_{seg/im}$), therefore, depends on the machine direction dimension (l_{im}^{MD}) of each image and desired cross section length (l_{cs}^{MD}). The number of segments can be calculated from the following equation.

$$n_{seg/im} = floor(\frac{l_{im}^{MD}}{l_{cs}^{MD}}) \tag{2.1}$$

where "floor (.)" is the function that takes as input a real number x and gives as output the greatest integer less than or equal to x. The image in Fig. 2.7 (a) is segmented in 2 parts (see image).

Multiple cross sections can be extracted from one segment. Number of extracted cross section from each segment can be expressed as

$$n_{cs/seg} = floor(\frac{l_{im}^{CD}}{l_{cs}^{CD}}) \tag{2.2}$$

Total number of extracted cross sections from each image ($n_{cs/im}$) can be expressed as

$$n_{cs/im} = n_{cs/seg} \times n_{seg/im} \tag{2.3}$$

320 cross sections are extracted in this manner from the image in Fig. 2.7 (a). Each cross section is analyzed using autocorrelation to extract the dominant wavelength and crepe frequency. The autocorrelation function of the cross section indicated in the image is shown in Fig. 2.7 (b). Again, the first peak (denoted by a blue circle) is detected to extract dominant wavelength (346 μm) and crepe frequency (73 folds/in.) of the cross section. Many other autocorrelation functions obtained from other cross sections are shown in 2.7 (c). It is readily seen that the shape of the functions are not similar to each other, rather vary from one cross section to another. All the autocorrelation functions are analyzed to first determine all the dominant crepe frequencies. The reported mean crepe count is calculated after ignoring the outliers that lie outside 2 standard deviation from the mean crepe frequency of all the cross sections. The histogram of dominant crepe frequencies of these cross sections (see Fig. 2.7(d)) is then constructed. Mean dominant crepe count (μ), standard deviation (σ), and the number of cross sections (n, after ignoring the outliers in the first calculation) are indicated in the histogram.

One very obvious advantage of the surface image based quantification is that a larger area of tissue, therefore many cross sections can be analyzed from one image. The amount of effort required to take one surface image is an order of magnitude lower than imaging one cross section. Therefore multiple images can be taken to analyze an even larger area which will give a more reliable estimate of dominant crepe count than cross section imaging.

Table 2.5: Mean dominant wavelengths and crepe counts of Grades 1-6 based on surface imaging

Name	CS per image, ($n_{cs/im}$)	Images (n_{im})	Mean dominant wavelength (μm)	Mean dominant crepe count (folds/in.)
Grade 1	400	6	685 ± 103	38 ± 7
Grade 2	400	6	548 ± 130	49 ± 12
Grade 3	320	5	261 ± 54	102 ± 22
Grade 4	320	5	326 ± 75	83 ± 22
Grade 5	320	5	264 ± 61	102 ± 24
Grade 6	320	5	346 ± 80	78 ± 21

2.3.3 Result

Grades 1-6 were analyzed using surface imaging technique. Mean and standard deviations of the dominant creping frequencies are tabulated in table 2.5. Number of images used for the analysis (n_{im}) and number of cross sections ($n_{cs/im}$) extracted from each image are also given. All the cross sections extracted are analyzed to compute the mean and standard deviations of creping wavelength and crepe count after excluding the outliers. Again, it is shown that Grade 1 and 2 have larger crepe folds compared to Grade 3-6. Also Grades 4 and 6 have larger crepe folds compared to Grade 3 and 5. The same observations were made from cross section quantification.

The detailed histograms are presented in Fig. 2.8 - 2.10 with a typical surface image. Again, 2 grades are grouped together for better presentation in one figure. For each grade, part of one typical surface image is shown (top) for visual interpretation. Machine and cross directions are indicated as "MD" and "CD" in the image. The actual images used for the analysis are larger in dimension. However, all the surface images shown here have the same dimension for better visual comparison. Comparing the surface images in Fig. 2.8 with Fig. 2.9 and Fig. 2.10, it is visually obvious that the Grades 1 and 2 have larger crepe folds compared to other grades. It is hard to distinguish the commercial grade images from one another visually. However, the histograms showing the distribution of crepe frequencies vary from one grade to another. Since the sample size of cross sections analyzed are sufficiently large (see n of each histogram), these distributions are more reliable and accurate. Again, the standard deviation of the creping wavelength and crepe count is seen to be considerably large, which comes from the large spatial variation of crepe folds. However, the nature of distribution is not explored in detail in this thesis. It can be seen that the histograms are not normally distributed, rather skewed (see histograms Grade 2, 4, and 6) like beta distribution or lognormal distributions. Therefore, other parameters like skewness can be determined to better represent these distribution on top of mean and standard deviation. In conclusion, the surface imaging method can distinguish the difference in mean dominant creping wavelength length scale among the grades and also give an estimation of variation of the creping frequencies. The dominant crepe count and corresponding variations from cross section imaging and surface imaging are compared in the next subsection.
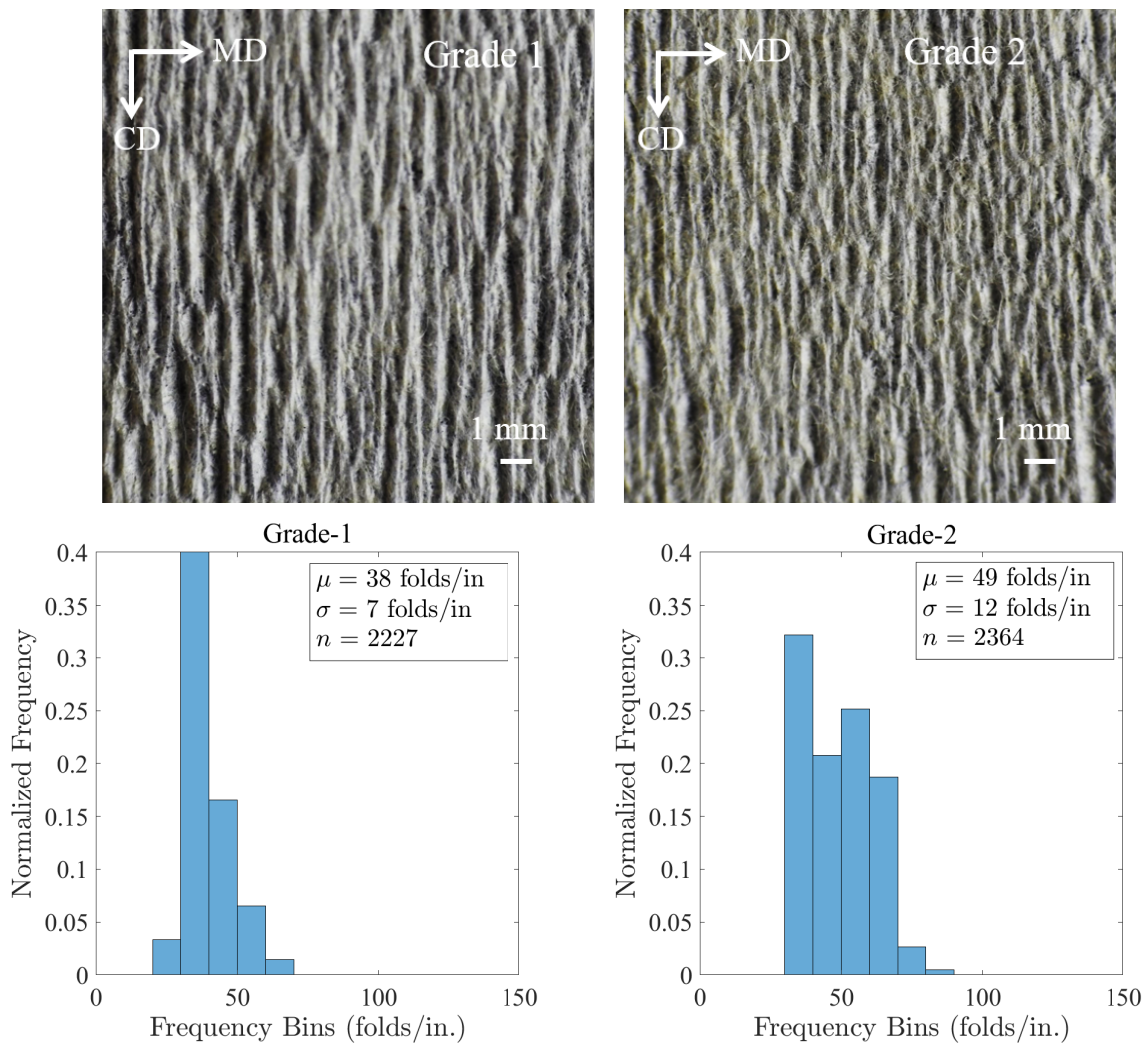
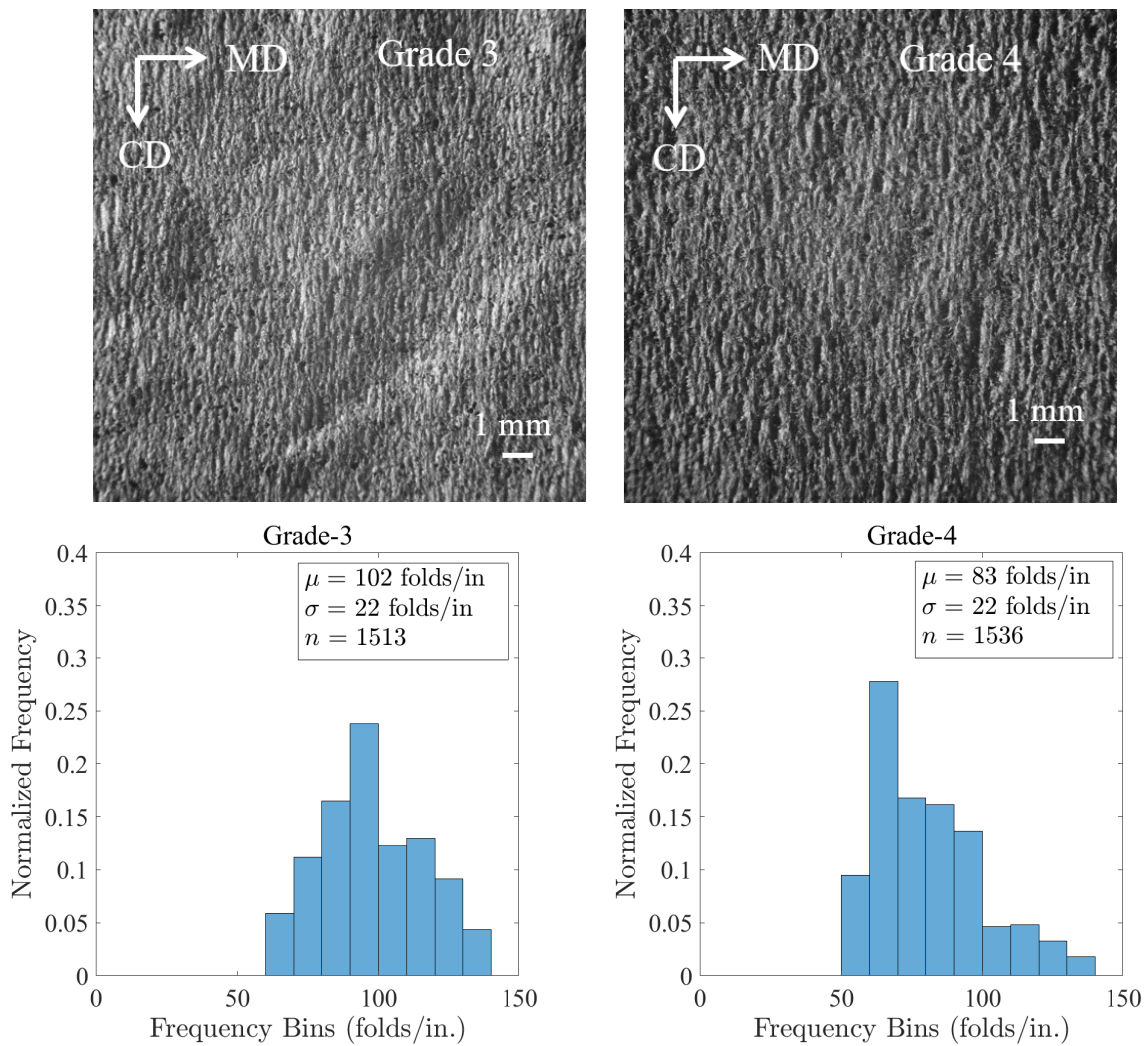**Figure 2.8:** Typical surface images and crepe frequency histograms for Grade 1 and Grade 2

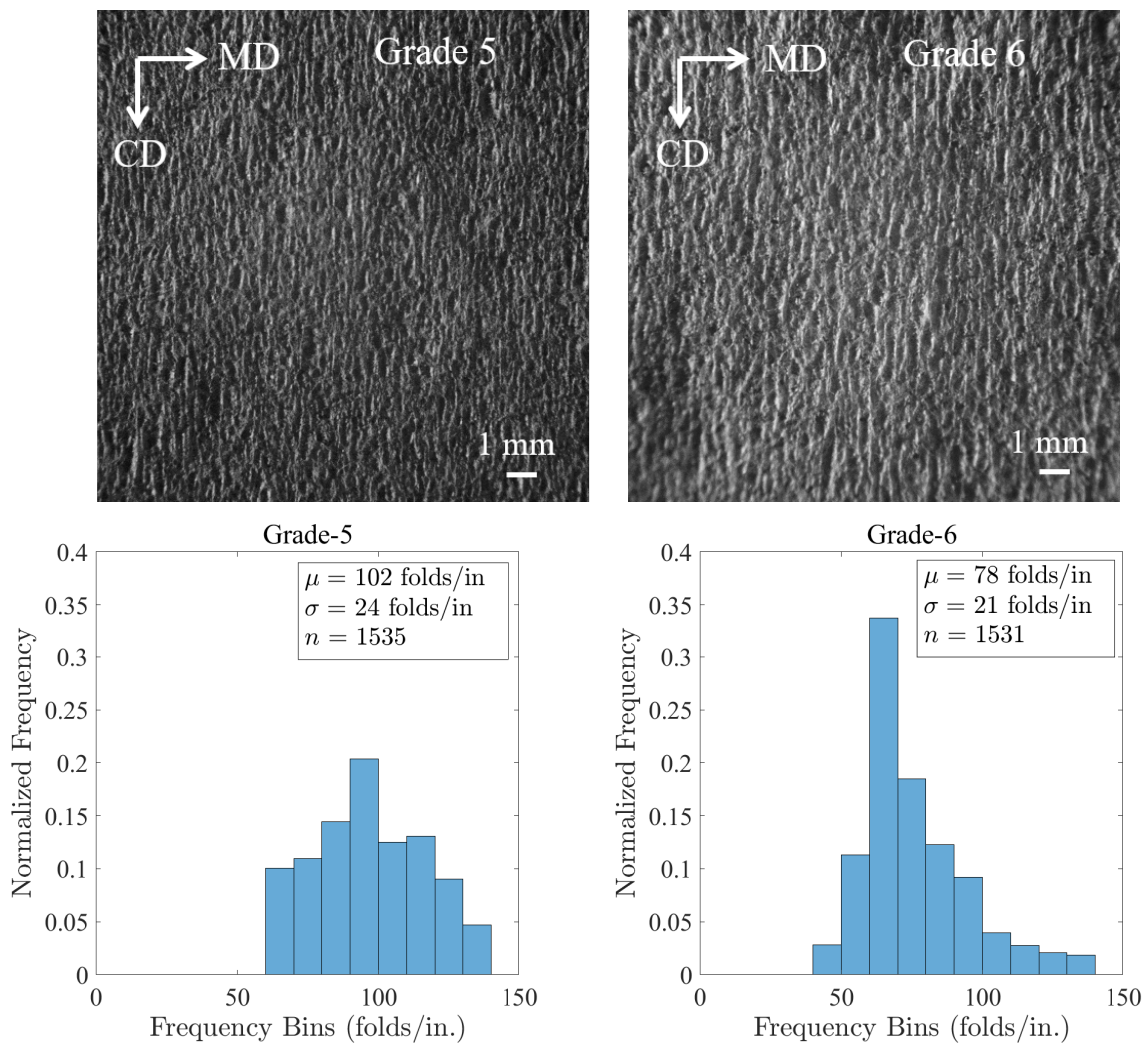**Figure 2.9:** Typical surface images and crepe frequency histograms for Grade 3 and Grade 4

Figure 2.10: Typical surface images and crepe frequency histograms for Grade 5 and Grade 6

2.4 Discussion and Conclusion

Fig. 2.11 shows the comparison of mean dominant crepe count between the through thickness and surface imaging technique. Surface image mean crepe count (Y axis) with corresponding variation is plotted against cross section imaging mean crepe count (X axis). High basis weight Grades 1 and 2 (marked in red circles) are separated from the commercial grades 3-6 (marked in blue squares). Good agreement of mean crepe count is found between the 2 techniques. Also the amount of variation in creping frequencies are approximately of the same order. A linear best fit of the data points is shown in a black dashed line, which deviates from the line of exact similarity (black solid line). An exact one to one correlation (x=y) should not be expected considering the stochastic behaviour of the folds. Also the cross section images and surface images are based on finite length of samples imaged at different parts (several meters apart) of the tissue. Considering these sources of variability, the agreement is acceptable, which establishes the capability of surface imaging to accurately measure mean crepe count.
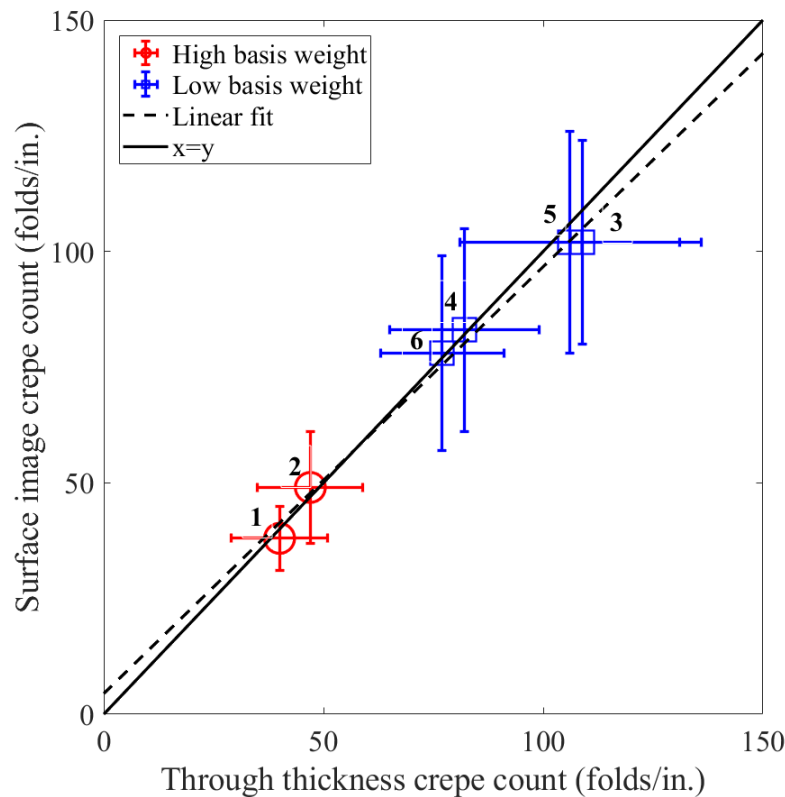

Figure 2.11: Through thickness and surface imaging crepe count comparison of Grade 1-6

Quantitative structural characterization of two high basis weight and four low basis weight tissue paper is done and compared. Significant conclusions are as follows.

1. A simple laboratory-scale experimental setup to capture crepe tissue surface images is developed. A systematic protocol of analyzing the surface images to extract quantifiable structural parameters of tissue, for example crepe count, is also established.

2. The results are compared with cross section imaging techniques for six different grades of tissues. The analysis proves that surface imaging is as accurate as cross section imaging based crepe count quantification. The added advantages of surface imaging over cross section imaging are its simplicity, robustness and possibility of statistical analysis for a more reliable quantification.

Chapter 3

Visualization and Online Measurement in Creping

The creped tissue structure visualization and quantification methods developed in Chapter 2 are used to visualize creping mechanism and quantify crepe structure online. Imaging experiments on creping have been done previously on a pilot tissue machine [5] and on a laboratory scale creping rig [9] to delineate the mechanism of crepe fold formation. However, yankee surface speed in both experiments was 140 m/min, which is about an order of magnitude lower than the real tissue machine yankee speed. In the current work, creping mechanism is visualized at a very high yankee speed ($>$ 1000 m/min) in a crepe simulator using a high speed camera and a line laser. The images are used to verify the creping mechanism at high yankee speed in section 3.1. Though mechanism of creping is believed to be well established among researchers, it was the first step towards confirming the mechanism at realistic creping speed.

Recently, other researchers have used very short duration pulsed light sources with machine vision cameras to capture tissue surface images and quantify crepe count in real tissue machine [18]. In this research, the surface imaging technique was integrated with a high speed flash to quantify crepe count in a tissue machine. Instead of a pulsed Laser Diode used by previous researchers, a simple, inexpensive high speed LED flash is used with a commercial DSLR camera. Tissue images were taken and quantified in a running machine over a three hour period. Tissue samples were collected during the experiment and quantified in lab to verify the crepe counts obtained online. Online measurements agree well with offline measurements. Details of the experiments are presented with results in section 3.2.

3.1   Visualization of Creping Mechanism

3.1.1   Experimental Setup

The lab-scale creping rig that was used to replicate and visualize creping at a high speed is shown in Fig. 3.1. It has five main parts; heated yankee cylinder, transfer roll, sheet moisture control system, an adhesive spray and an instrumented creping blade. The sheet moisture control system and adhesive spray are not shown in the figure. Details of each part are given below.

- Yankee : A cast iron shell of 16 in. diameter. Heating is provided internally.
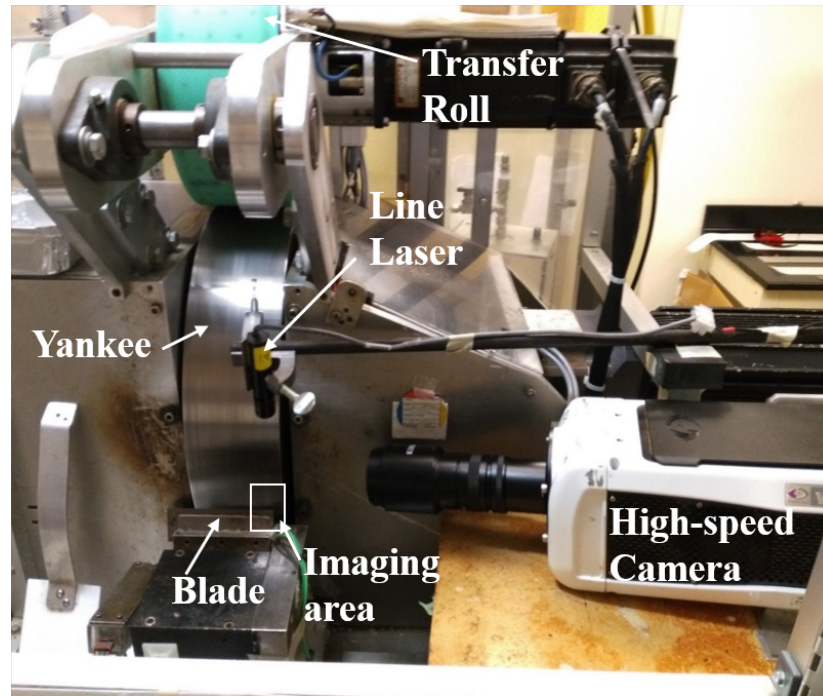
Figure 3.1: Creping rig with high speed cross-section imaging setup

- Transfer roll : Green coloured roll above the yankee. It is used to transfer the wet sheet to yankee.

- Sheet moisture control system (not shown in figure) : A mechantronics system used to set the moisture content of sheet at desired level.

- Adhesive spray (not shown in figure) : Sprays controlled amount of adhesive to yankee surface.

- Instrumented crepe blade : Section of a standard crepe blade with a 3D force transducer mounted on a fixture.

The yankee keeps dwelling at very low (2 rpm) speed to maintain a uniform surface temperature. The temperature can be varied from room temperature to an excess of 130°C. At the beginning of each experiment, an uncreped sheet is applied to the transfer roll and brought to the desired moisture content. The sheet length is about 27 in. A preset amount of coating package (a mixture of adhesive, release agent, modifier and plasticizer) is sprayed onto the yankee drum simultaneously. The transfer roll presses and transfers the sheet on the yankee after a preset amount of curing time. At this stage the yankee starts to rotate at higher speed and

when a desired yankee speed is reached, the creping blade is engaged to crepe the sheet from yankee surface. The device is capable of speeds up to 1524 meter/min and can be used with any basis weight sheet from low to high. A 25 gsm paper sheet of 63.9 μm caliper was creped at 1120 m/min for the experiment. Creping angle was set to 80°. A line laser was used to illuminate a cross-section of tissue very close to right edge. The imaging area is shown in Fig. 3.1. A high-speed camera was used to capture the creping mechanism at 67000 frames per second. The camera was triggered by the force sensor attached to the blade to capture the creping mechanism.
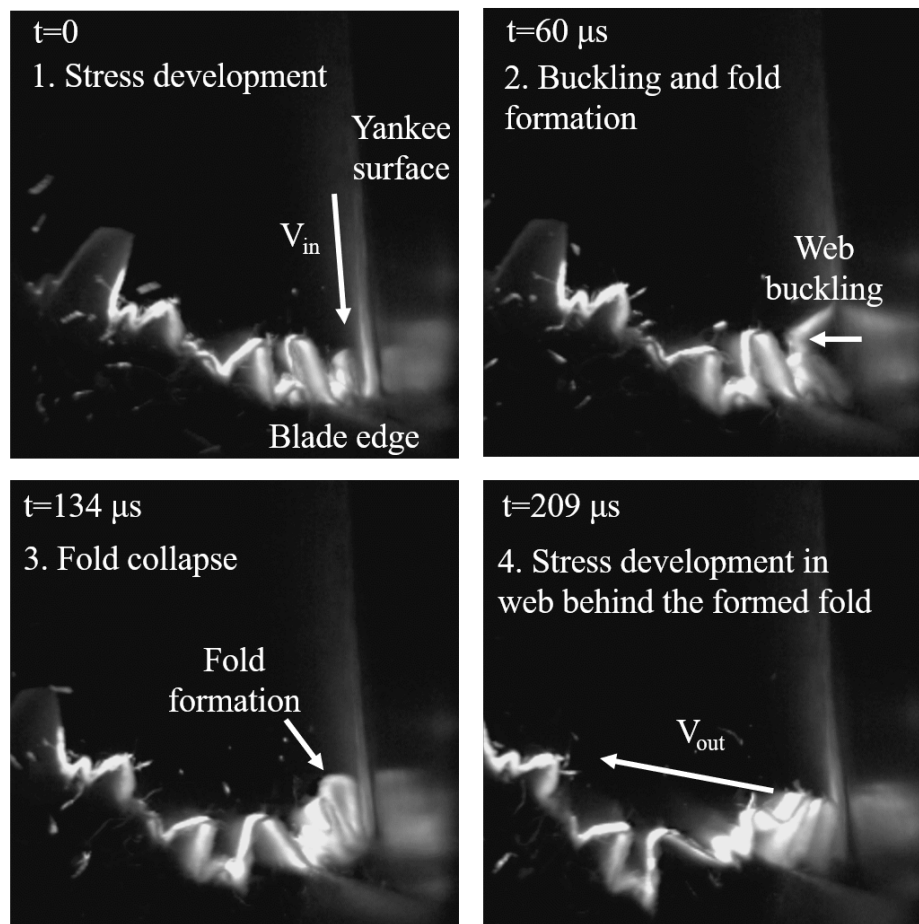
3.1.2 Creping Mechanism

Figure 3.2: Four stages of creping fold formation in the high speed creping rig

Fig. 3.2 shows four images corresponding to four stages of fold formation captured in the experiment. In the first stage, paper sheet hits the blade edge as shown in 1. The sheet buckles and forms a fold in stages 2 and 3. Then the fold gets pushed off the edge and the process repeats. This mechanism is similar to the well established mechanism found in literature [5, 7, 9, 10] . However, there are some limitations. Imaging of the tissue was done at edge of the paper. It was later observed that the crepe folds towards the edges were larger in size compared to the crepe folds in the middle. Therefore the folding observed may not be exactly representative of folding in midsection.

3.2 Online Crepe Structure Quantification

The surface image quantification technique developed in Chapter 2 is integrated with a high speed static imaging system to measure crepe count online in a real tissue machine. Images of crepe tissue surface were captured at regular intervals for 3 hours and analyzed online using the surface image analysis technique developed in section 2.3.2. Tissue samples were collected during the experiment for offline crepe count analysis. Crepe count measurement from both online and offline imaging were compared to verify the accuracy of quantification based on online images.

3.2.1 Experimental Setup

The experiments were carried out in a paper machine of a tissue manufacturing plant. Fig. 3.3(a) shows the high speed imaging set-up placed between the yankee drum and reeling section of a paper machine inside the plant. Images of tissue were taken under a sheet stabilizer to avoid sheet-fluttering. Fig. 3.3(b) shows the components of the high speed imaging setup. It has three main components: a commercial Digital Single Lens Reflex (DSLR) camera (Nikon D 7000), a high speed Light Emitting Diode (LED) flash (Vela one) and a small table fan placed inside a box. The high speed flash is synchronized with camera via a wireless triggering system. The flash can illuminate the tissue surface with a high intensity pulse of light for 1 microsecond. This short intense burst of light limits sheet movement to about 15 microns for a tissue machine operating at 1000 m/min.

High speed camera was not used for this type of imaging. The dusty, steamy environment around the imaging area makes it impossible. Further, the narrow space available for imaging is very small to accommodate the intense diffuse light and wires needed for the high speed camera to work. The entire system with DSLR camera is compact and capable of wirelessly transmitting the captured images to a laptop placed outside the tissue machine. Whole box is covered except the top of lens to protect the equipment from dust and humidity. A small fan is used for circulation of air to prevent moisture condensation and dust buildup as shown in Fig. 3.3(b).

Figure 3.3: Online crepe count quantification setup in a real tissue machine (left). Components of the high speed imaging setup (right).

3.2.2 Result

Fig. 3.4 shows the variation of crepe count with time, over a 3 hour window. Several online images were taken at regular interval of approximately 15 minutes. They were analyzed using surface image quantification method explained in section 2.3.2. Mean dominant crepe counts extracted from those images are plotted against time in blue circles. The errorbars at each data point represents the standard deviation in crepe frequency of each image. The variability comes from the spatial variation of crepe fold length scale in one image, which is a property of the image and not a measurement error. The measured mean dominant crepe counts are repeatable (see the close cluster of mean dominant crepe counts at different times intervals). It can be seen that the dominant crepe count is around 90 folds/in., which is typical for a commercial grade tissue. Several sample of tissue were collected at different times during the experiment for offline analysis. They were analyzed offline using the surface imaging setup described in section 2.3.1. Offline results are plotted at the time they were collected in the experiment in red squares on the same plot. It can be observed that the crepe count obtained offline are similar to mean crepe count measured online. It is not realistic to expect exactly similar numbers because the images analyzed are not taken exactly at same area of tissue, but probably several thousand meters away from each other. Also during online imaging, the sheet is under tension for reeling. Exact value of this tension is unknown and may change the crepe structure slightly when
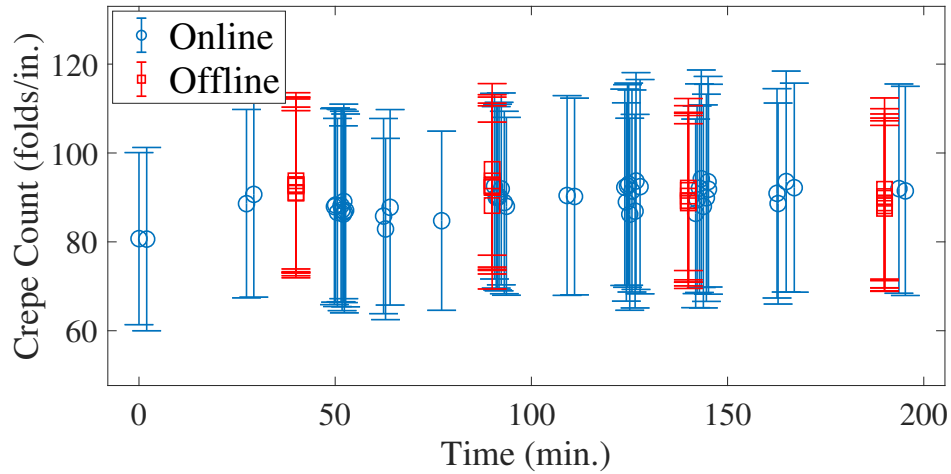
Figure 3.4: Comparison of online and offline mean dominant crepe count, and standard deviation with time. The standard deviation at each data point is shown as a two sided vertical error bar. This variation represents the spatial variability of crepe fold length scale in one surface image, and not related to measurement accuracy.

detached from tissue machine and reeled. With these factors in consideration, the agreement is within the statistical dispersion. This leads us to believe that the surface imaging technique is capable of quantifying crepe count from images taken at high speed.

3.3 Conclusion

High speed video and static imaging techniques are used to visualize and quantify creping in this chapter. Significant conclusions are as follows.

1. For the first time, mechanism of creping is observed through the thickness of a tissue paper at a speed over 1000 m/min in a realistic creping rig. However The mechanism is observed at the edge of tissue paper, which is generally loosely bonded to the yankee drum. The same technique can be used in future to observe creping at the middle portion of the tissue.

2. The laboratory scale surface imaging technique (see Chapter 2) is successfully integrated with the high speed flash to measure crepe count during production in a real tissue machine. The potential of this device to work as an inexpensive online process monitoring tool is significant.

Chapter 4

Tensile Response of a Creped Tissue

4.1 Introduction

The tensile testing of tissue papers is ubiquitous among tissue manufacturers, who use it for quality control. For manufacturers, the strength and stretch of tissue are important parameters whereas they pay little heed to the shape of the tensile curve. Sufficiently high dry and wet tensile strength along the machine and cross direction are crucial to ensure tissue machine runnability and successful conversion or embossing operations. High stretch and low elastic modulus along machine direction is important to obtain a softer (bulk softness) tissue. However, there is a trade-off between strength and softness. Tissues with higher softness tend to be weaker. Therefore, to create a sufficiently strong tissue structure with high softness, a basic understanding of the deformation mechanism and failure mode of tissue fiber network is needed. In section 4.2 of this chapter, stress strain response of low density commercial grade tissue papers (Grade 3-6) is determined along both machine and cross direction. Tensile strength, breaking stretch and initial Young's modulus are quantified according to existing standard [2] from the stress strain data. In another experiment, the fiber network is imaged under a microscope during tensile testing to observe the deformation of the network structure and failure mode in section 4.3. Crepe folds structures in tissue are believed to decrease stiffness of paper materials along machine direction. Investigation of crepe fold deformation with machine direction tensile loading can give insight into the network stiffness at low strain, which is related to bulk softness of tissues. Therefore, evolution of crepe fold structure with machine direction tensile load is quantified in section 4.4. Fiber-fiber bond strength is known to govern tensile strength of paper [23]. It has been reported that large local strains are precursors to bond failure [24]. In low density paper like tissue, large strain localization can occur due to various reasons like sparse fiber network, and poor formation. Analysis of principal strain field at various global network strain is done along machine direction to quantify the uniformity and observe the degree of strain localization in 4.4.

4.2 Tensile Characterization

4.2.1 Experimental Setup

The experimental setup to determine in-plane uniaxial tensile stress strain behaviour of tissue samples is shown in Fig. 4.1 (a). An INSTRON 5969 universal testing machine is used in tensile
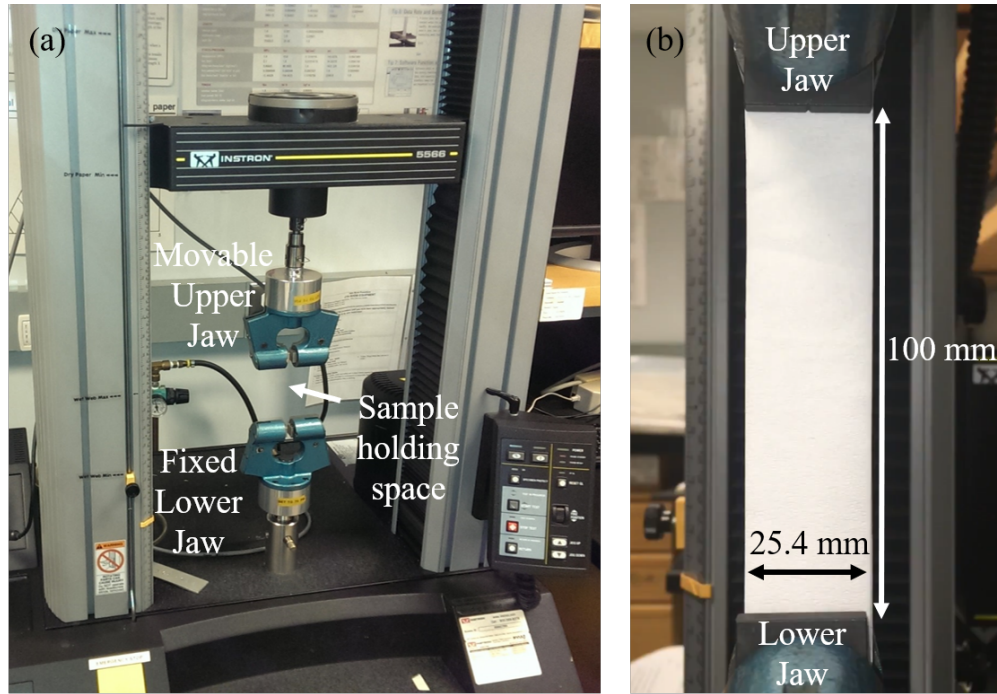
Figure 4.1: (a) Experimental set up for tensile test of tissue papers. (b) Dimension of tested tissue samples. Tests are done according to ISO: 12625-4 protocol [2]
.

testing mode to do the experiments. The machine is equipped with two pneumatic pressure jaws to hold the tissue samples firmly while applying tensile strain. A rubber coating is used on the inner face of each jaw to avoid any slippage during the test. The bottom jaw is fixed to the base of the machine while the top jaw can move upwards at a constant velocity (1-100 mm/min) to strain the samples. An encoder is used to measure the upper jaw displacement. A 500 N load cell (0.5% accuracy at 0.5 N) is attached to the top jaw to measure load. Both displacement and load are measured and recorded simultaneously in real time for postprocessing.

Tensile response of paper products can vary with dimensions of the sample [27], strain rate, sample defects, formation, moisture content and temperature [28]. Humidity and temperature of the testing environment can also affect the results. Consistency of all these parameters is of immense importance for repeatability and consistency of each test. ISO 12625-4 tensile test protocol for tissue papers is followed for these tests [2].

15 samples along both machine and cross direction, each 150 mm long and 25.4 mm wide, were prepared beforehand for tensile tests. The width of the samples were not 50 mm as prescribed in the protocol because the jaws of the INSTRON machine were only 25.4 mm wide.

However, this change was acceptable as per protocol as long as mentioned in the report. A single edge paper cutter was used to cut the samples from parent roll. For preconditioning, the samples were kept at the testing environment at 23°C and 50% relative humidity for 48 hours before testing. Samples were examined to eliminate any specimen with obvious defects in the testing area. Though 150 mm long samples were prepared, only 100 mm was used as gauge length. 25 mm from top and bottom of the sample was used to grip the samples by pneumatic jaws. To eliminate any slack in the tissue, each sample was preloaded with 5 N/mm force. The samples were elongated at a uniform extension rate of 50 mm/min. At this extension rate, the inertial effects on the load extension plots are negligible. 10 specimen from each grade were tested for statistical robustness.
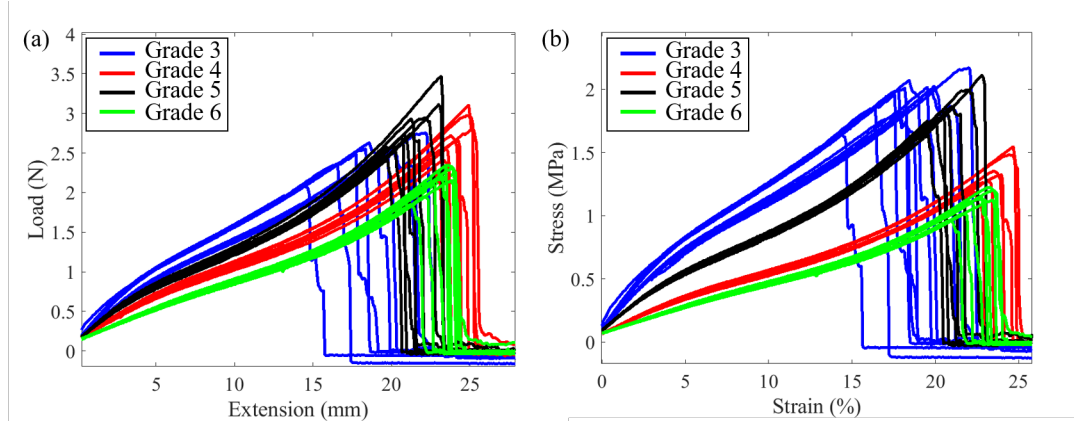
4.2.2 Results

Figure 4.2: Load extension (a) and corresponding stress strain plots (b) for multiple samples of Grade 3-6 along machine direction

Table 4.1: Analysis results of the machine direction load extension and stress strain plots shown in Fig. 4.2

Name	Stretch at break (%)	Tensile strength (N/m)	Initial modulus (MPa)	Tensile energy absorption (J/m^2)
Grade 3	18.32 ± 2.02	97.95 ± 7.05	15.81 ± 1.33	10.17 ± 1.49
Grade 4	23.89 ± 0.88	107.14 ± 9.11	6.13 ± 0.27	12.34 ± 1.13
Grade 5	21.14 ± 1.13	111.76 ± 11.56	10.92 ± 0.47	11.62 ± 1.44
Grade 6	22.72 ± 0.81	85.4 ± 6.07	4.32 ± 0.14	9.26 ± 0.81

Fig. 4.2 shows the load extension (left) and stress strain (right) plots for Grade 3-6 along
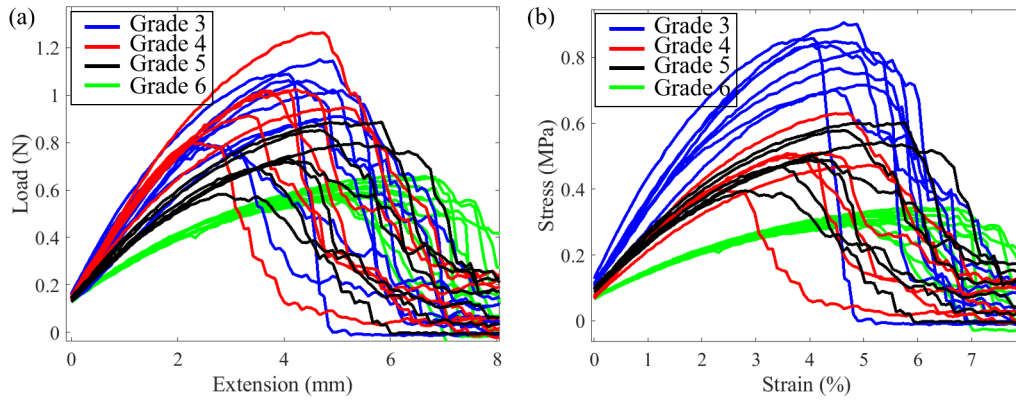
Figure 4.3: Load extension (a) and corresponding stress strain plots (b) for multiple samples of Grade 3-6 along cross direction

Table 4.2: Analysis results of the cross direction load extension and stress strain plots shown in Fig. 4.3

Name	Stretch at break (%)	Tensile strength (N/m)	Initial modulus (MPa)	Tensile energy absorption (J/m^2)
Grade 3	4.2 ± 0.69	38.89 ± 4.13	22.52 ± 1.81	1.14 ± 0.25
Grade 4	4.02 ± 0.81	37.99 ± 5.09	14.42 ± 1.87	1.06 ± 0.31
Grade 5	4.36 ± 0.85	30.08 ± 3.5	13.95 ± 1.22	0.94 ± 0.3
Grade 6	5.5 ± 0.7	23.74 ± 1.33	7.04 ± 0.24	0.96 ± 0.18

machine direction. Load at zero extension is positive because of preloading to eliminate slack in the samples. Stress strain plots are calculated from the load extension data. Stress is calculated as load per unit cross-sectional area of the undeformed sample. Cross section area of unde-formed sample is calculated from the caliper and width of tissues. Strain is the extension of the sample divided by the gauge length. Tensile behaviour of tissue papers shows significant non-linearity along machine direction for all grades. Along machine direction, the tensile response has three stages of nonlinearity as seen in Fig. 4.2 (a) and (b). It begins with a initial elastic region (approximately before 2% strain) followed by a strain-softening region (approximately 7% - 12% strain) and finally a hardening region towards the end before failure. Explanation of the exact reasons of these transitions is out of scope of this thesis. However, a partial answer will be given in subsequent sections. All grades show a variation in breaking strength and breaking stretch close to the end of the test. This is believed to be a result of the inherent sparse nature of the fiber network and fiber fiber bonds, which govern the strength of the tissue. Grades with uniform formation and good quality fibers should show less dispersion with that argument and grades with poor formation and low quality fibers should perform poorly in terms of repeatabil-

ity. From Fig. 4.2, it can be seen that Grade 3 has more dispersion in stretch at break and over all shape compared to other grades. It was confirmed from the relevant industry that Grade 3 was indeed a low quality tissue grade. The shape of stress strain plots along machine direction are fairly consistent and repeatable within other grades.

Load extension and stress strain data are analyzed to extract **tensile strength** (N/m), **stretch at break** (%), **initial modulus** (MPa) and **tensile energy absorption** (J/m^2). Tensile strength is the highest load carried by the sample per unit width. This load occurs generally just before the onset of fracture of samples. The higher the tensile strength, the stronger is the tissue. The strain at the breaking load is known as stretch at break. Tensile energy absorption is the work needed to break the sample per unit area of the undeformed sample. It is the area under the load extension plot until failure divided by the undeformed area of the sample. Initial modulus is calculated as the slope of the stress strain plot between 0% and 2% strain. The mean and standard deviation of these parameters for all grades are tabulated in Table 4.1. From Table 4.1, it can be seen that Grade 3 shows higher variation in all the four parameters compared to other grades, which reiterates the fact that formation and quality of fibers are important to produce a high quality and consistent tissue.

Similar tensile characterization is done along cross direction. The load extension and stress strain plots are shown in Fig. 4.3 (a) and (b). The analysis results are tabulated in Table 4.1. In cross direction, the tissue paper shows monotonic progressive softening behaviour with load (see Fig. 4.3) with more visible dispersion in the entire shape for all Grades, except possibly for Grade 6. This shape is entirely different than the machine direction tensile response, which indicates that crepe folds govern the shape of the tensile response. Crepe folds do not contribute in the tensile response along cross direction since they are aligned perpendicular to the direction of applied load. Therefore, the shape of tensile response along cross direction is entirely governed by formation and furnish of tissue.

Comparing Table 4.1 and 4.2, it can be concluded that stretch at break in machine direction is higher than cross direction for all 4 grades. The machine direction stretch is higher than cross-direction stretch because creping compresses and packs more material as series of folds in machine direction. While load is applied, these folds are removed which gives rise to the high stretch. Also the tensile strength is higher along machine direction because of preferential alignment of fibers along machine direction during formation. Because of high stretch at break and strength, the tensile energy absorption is also higher along machine direction. However, the initial modulus in machine direction is lower than cross direction. Creping folds are believed to cause this deterioration of modulus along machine direction. The role of creping folds on the overall physics of tensile deformation, specially in the low strain region will be explored in section 4.4.2.

4.3 Visualization of Fiber Network Deformation

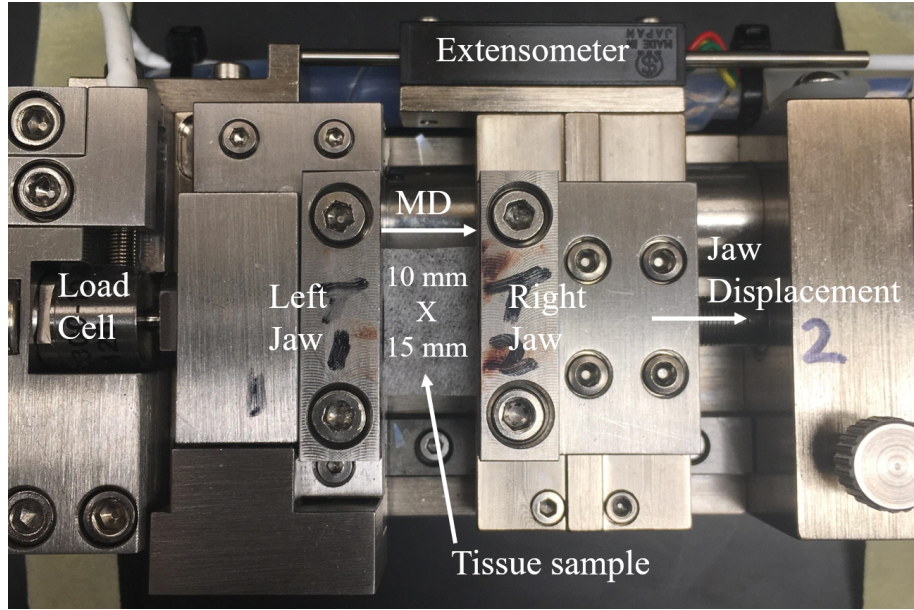### 4.3.1 Experimental Setup

Figure 4.4: Microtensile stage (DEBEN Microtest 200N Tensile Tester; Serial number : MT10129) for tensile test of tissue paper outside SEM chamber

Further experiments are done to observe the deformation and failure mechanism of the fiber network under machine direction load. A microtensile tester (DEBEN Microtest 200N Tensile Tester; Serial number : MT10129) with *in situ* SEM imaging capability is used for this experiment. Fig. 4.4 shows the microtensile stage outside SEM chamber with attached tissue sample ready to test. Tissue samples were cut from parent roll using a single edge blade and no preconditioning was done in this experiment. Each sample had a gauge length of 10 mm along machine direction and 15 mm width along cross direction. After carefully attaching the sample to the device, the entire setup was placed inside an SEM chamber and the sample was elongated at 2.37 mm/min (see AppendixA for calibration details) until failure. Entire load-extension plot was recorded with a video of the tissue sample until failure. About 1 mm^2 area of the sample was visualized to observe the deformation.

4.3.2 Results and Observations

Fig. 4.5 - 4.8 shows the deformation of tissue's fiber network with load for all grades. Images at 3 different stress levels ((b)-(d)) along with post failure images (e) of tissue samples are shown
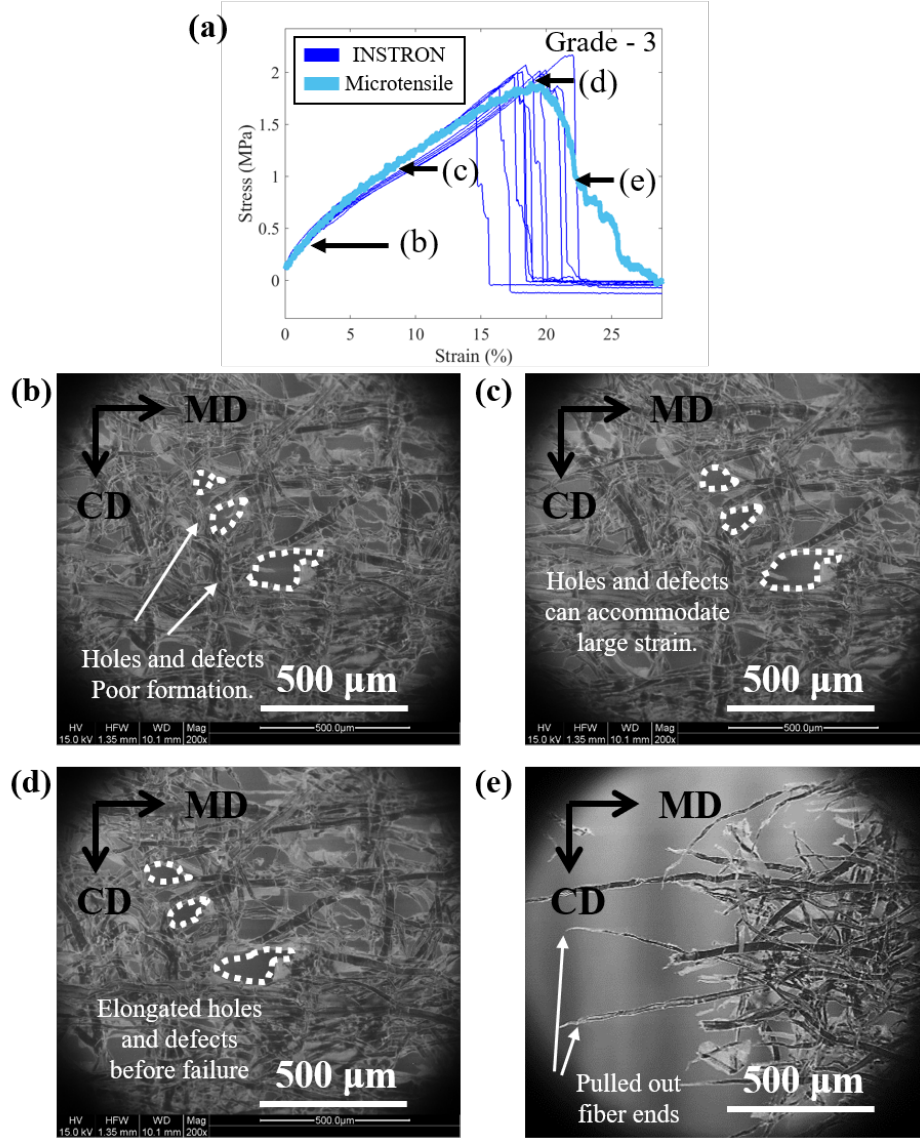
Figure 4.5: Microscopic deformation of tissue fiber network under tensile load for Grade 3. Tissue microstructure at approximately end of elastic region (c), at half of breaking strain (c), at breaking strain (d) and after network failure (e). Approximate locations of these pictures on stress strain plot are shown in top.

Figure 4.6: Microscopic deformation of tissue fiber network under tensile load for Grade 4. Tissue microstructures at approximately end of elastic region (b), at half of breaking strain (c), at breaking strain (d) and after network failure (e) are shown. Approximate locations of these pictures on stress strain plot are shown in top.
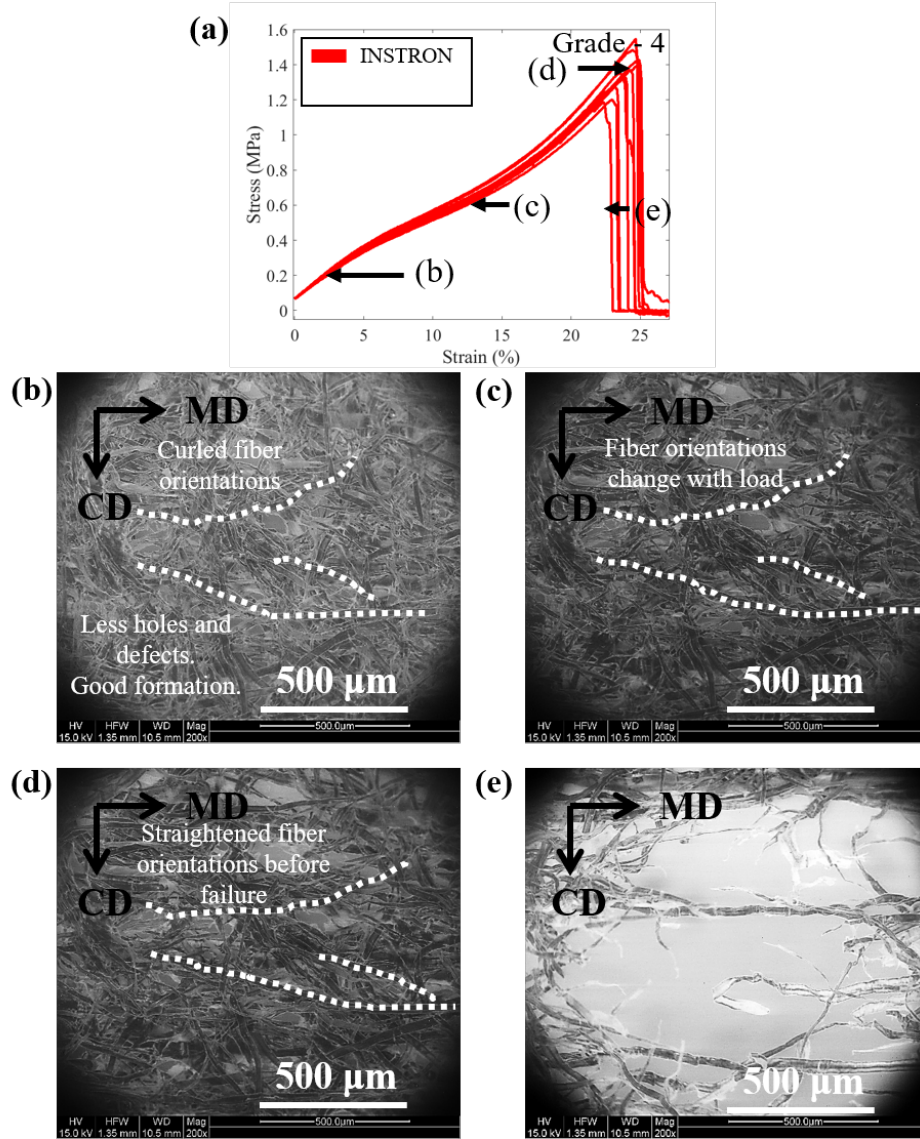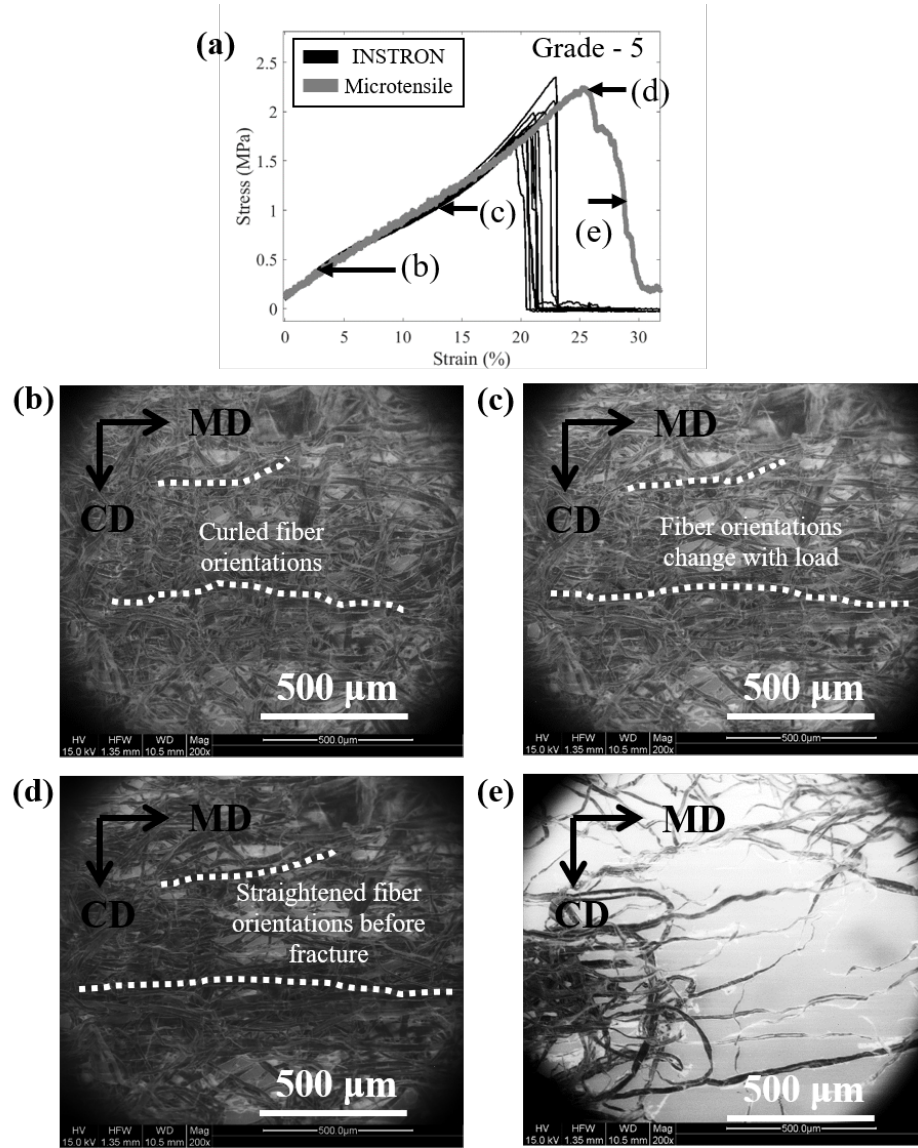
Figure 4.7: Microscopic deformation of tissue fiber network under tensile load for Grade 5. Tissue microstructures at approximately end of elastic region (b), at half of breaking strain (c), at breaking strain (d) and after network failure are shown. Approximate locations of these pictures on stress strain plot are shown in top.

Figure 4.8: Microscopic deformation of tissue fiber network under tensile load for Grade 6. Tissue microstructures at approximately end of elastic region (b), at half of breaking strain (c), at breaking strain (d) and after network failure (e) are shown. Approximate locations of these pictures on stress strain plot are shown in top.
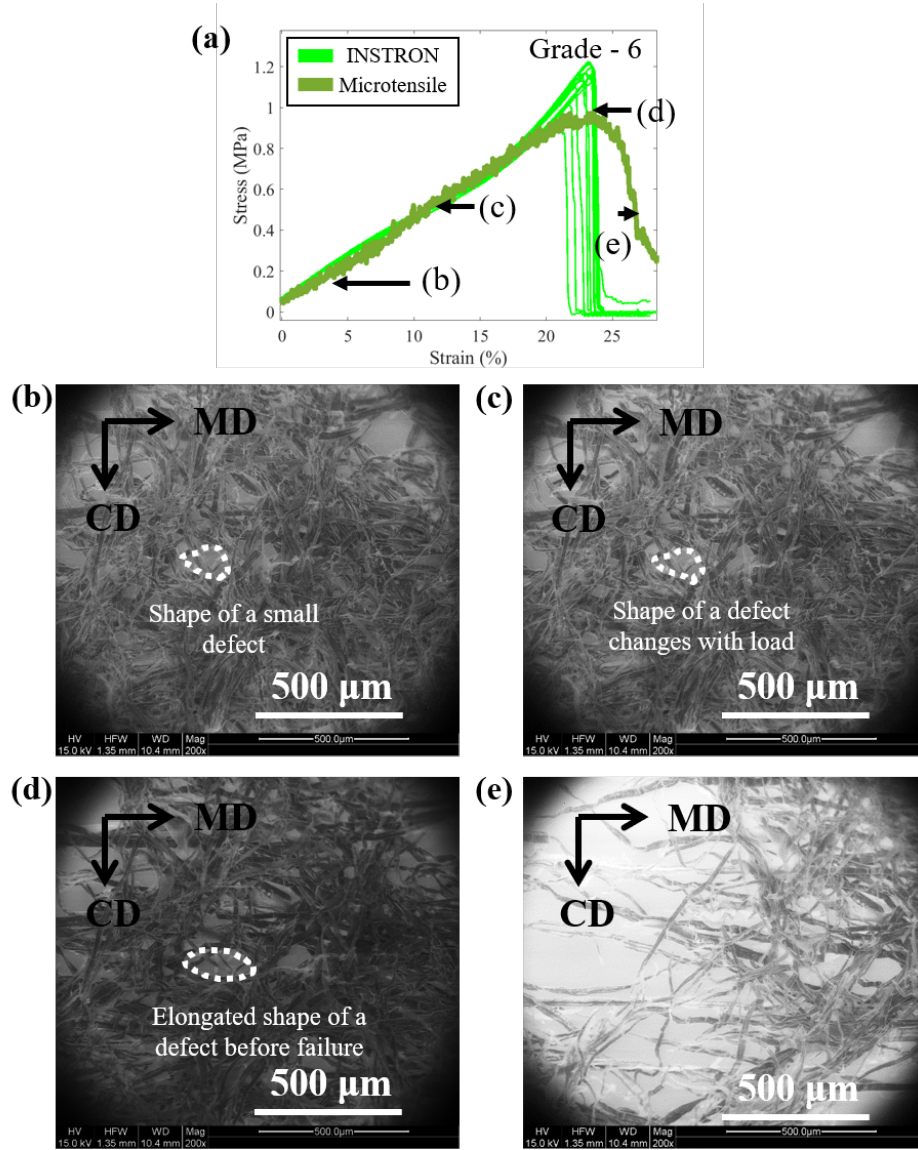
for all grades. Approximate state of stress and stain of the entire tissue sample for each image is marked in the stress-strain plot above. There stress strain plot from the microtensile stage is compared with the family of characteristic tensile response (obtained from INSTRON as shown in Fig. 4.2) of each grade in Fig. 4.5 (a) - 4.8 (a) first and the locations of the images are marked on the microtensile stage data. Stress strain plots from the microtensile stage are shown for all grades, except for Grade 4 (Fig. 4.6 (a)) in which no data was obtained from the device unfortunately. However, approximate locations of images are shown on the INSTRON stress strain plot in this case. Though the testing environment inside the SEM (ambient temperature and 5% relative humidity), sample size and strain rate were different in these experiments, the stretch, strength and shape of tensile curve were similar to the characteristic tensile response until fracture, confirming similar mechanism of deformation. On careful observation, one might see that the stress strain data obtained from the microtensile stage is very noisy. This is because of the inferior load cell accuracy of the microtensile stage compared to the load cell attached to the INSTRON machine.

Though the shapes of the curves are similar, the post failure behaviour is significantly different. The drop in load upon fracture is much abrupt in INSTRON than the microtensile stage. This is explained by the strain rate in each experiment. In INSTRON, the tissue samples were strained at a strain rate of 50% / min (50 mm/min extension rate at 100 mm gauge length). In the microtensile stage the samples were strained at a much lower strain rate of 23.7% / min (2.37 mm/min extension rate at 10 mm gauge length). Because of a lower strain rate, the fracture propagated slowly showing a less abrupt load drop after failure.

Images obtained from the SEM can show the quality of formation of each grade. Grade 3 has a more porous structure compared to other grades as seen in Fig. 4.5 (b) as a result of poor formation. This is also confirmed by the industry and discussed in Section 4.2.2 before. These holes and pores in tissue network can deform to a large extent to accommodate large strain around them. Evidence for this phenomenon is shown in Fig. 4.5 (b) - (d) and also in 4.8 (b) - (d) for another grade. The indicated holes (surrounded by white dashed lines) in those pictures change shape and size until failure to distribute the strain concentration around them. Other than this, curled and kinked fibers are shown to be straightened out with load in Fig. 4.6 (b) - (d) and 4.7 (b) - (d). Some fibers are indicated as white dashed lines. Based on these observations of the tissue deformation, it can be concluded that the fiber network can undergo significant rearrangement of to accommodate large strain. It can be seen that the flexible fiber fiber bonds rotate and slide to rearrange the network and also the curled fibers are straightened towards the end of the tensile curve, but prior to fracture. Straight fibers are much stiffer than curled fibers, and this stiffens the entire network before fracture. This argument qualitatively explains the hardening of the tissue before failure in machine direction. Also it is observed that very few fiber fiber bonds rupture during the straining process. However at failure, the inter fiber bonds fail together abruptly, resulting in the failure of structure. Pulled out unbroken fibers can be seen clearly in the post-fracture images of Fig. 4.5 (e). Creping folds are not distinguishable in any of these images and how these folds behave under tensile load is not clear from this experiment.

4.4 Structural Evolution with Load

4.4.1 Experimental Setup

To observe the evolution of crepe folds, one tissue specimen from each grade was loaded in the machine direction in small load-steps (approximately 0.1 N) and imaged at each step with oblique diffuse light to highlight the crepe structure. The experimental setup for surface imaging described in section 2.3.1 is used to image tissue surface at each load step. The pulley and weight system of the setup is used to load the samples using calibrated weights. The loading is done slowly to avoid any sudden impact-load on the structure. Once loaded, the tissue is allowed to relax for 30 seconds to reach the maximum elongation, at which point the surface images are taken. Length and width of each tissue sample specimen are 100 mm and 25.4 mm respectively. These tissue samples are not preconditioned in a constant temperature and humidity environment, and the experiments are done at ambient temperature and humidity. Stress strain plots obtained from these experiments are compared with the characteristic tensile response to validate each test.

4.4.2 Evolution of Crepe Structure and Local Strain Field

Tensile evolution of crepe folds and local strain field are shown in Fig. 4.9-4.12. Each figure corresponds to a separate grade. Stress strain plots were constructed for all grades from the applied load and calculated global extension. Graph (a) in each figure shows the stress-strain data (discrete loading since weights were applied in steps) obtained from the experiment superimposed on the characteristic stress-strain plot obtained from previous tensile characterization experiment in section 4.2.2. In Fig. 4.11, the breaking strain in discrete loading experiment for Grade 5 is almost half of the characteristic breaking strain. This indicates that the sample broke prematurely, which invalidates the experiment. The stress strain plot obtained from discrete loading for other grades reach similar breaking stress and strain as the characteristic response, but shows a systematic deviation. More specifically, the strain in discrete loading experiment, is higher than the characteristic strain at a given load. This happens because tissue paper is a viscoelastic material [29, 30] and slowly stretches with time if left under a constant load. In these experiments, photo of the tissue surface was taken at least 30 seconds after the load was applied. This time difference caused the tissue to elongate more and give a higher strain than expected. With this in mind, the agreement between the stress strain plots is satisfactory. 3 data points ((b) - (d)) are highlighted in each these plots in Fig. 4.9 (a) - Fig. 4.12 (a) and the analysis results of the corresponding surface images are shown below.

At each step of (b) - (d), a 2D Fourier Transformation of the surface image (left) and the principal strain field (right) are shown. Fourier Transformation of the reflection images show the frequency distributions of the crepe fold structure and wire mark patterns along machine and cross directions. These are indicated in each figure. 2D FFT of the surface image at low

Figure 4.9: Evolution of crepe structure in 2D Fourier space (bottom left) and local principal strain field (bottom right) with increasing machine direction tensile load approximately at the end of elastic region (b), half of breaking strain (c) and at breaking strain (d) for Grade 3. Global stress and strain associated with each step are shown in the stress strain plot above.
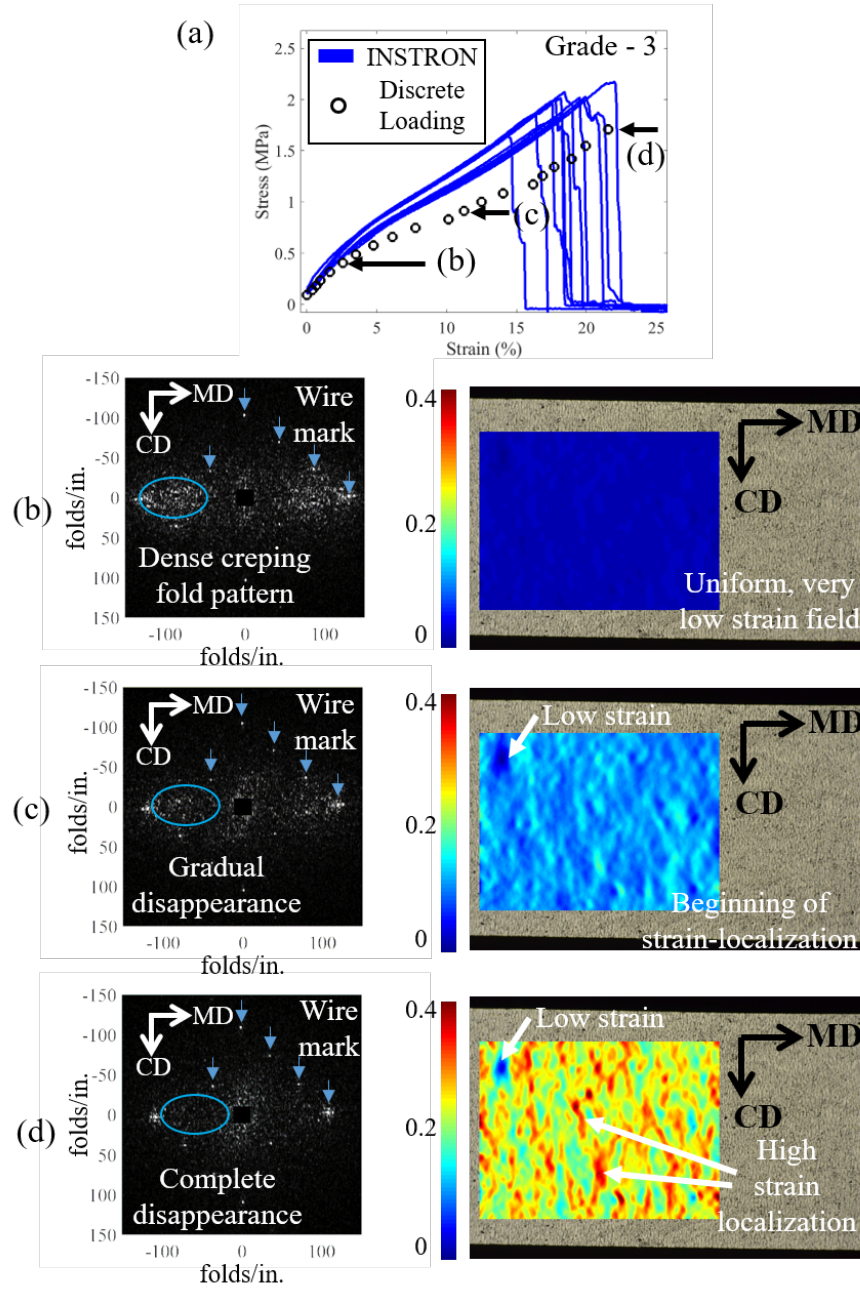
Figure 4.10: Evolution of crepe structure in 2D Fourier space (bottom left) and local principal strain field (bottom right) with increasing machine direction tensile load approximately at the end of elastic region (b), half of breaking strain (c) and at breaking strain (d) for Grade 4. Global stress and strain associated with each step are shown in the stress strain plot above.
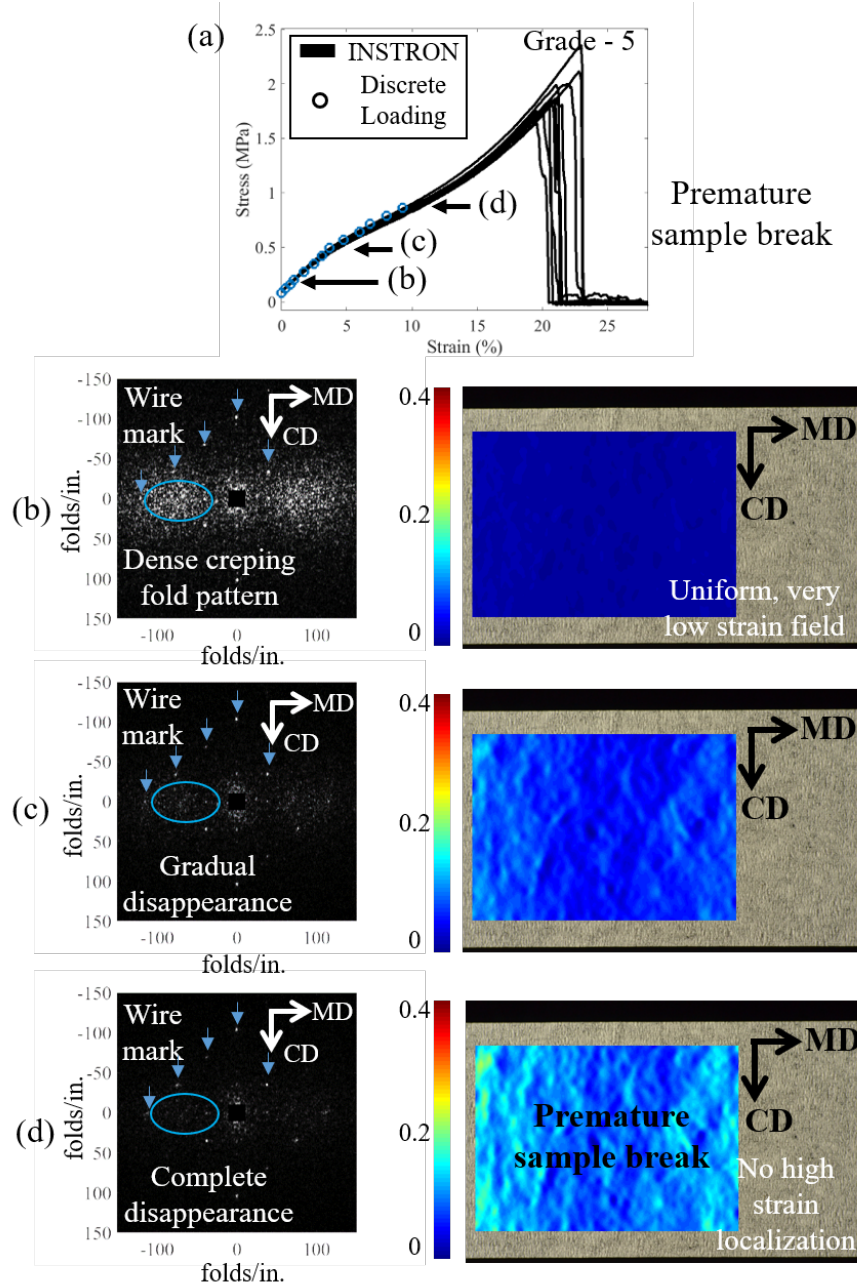
Figure 4.11: Evolution of crepe structure in 2D Fourier space (bottom left) and local principal strain field (bottom right) with increasing machine direction tensile load approximately at the end of elastic region (b), half of breaking strain (c) and at breaking strain (d) for Grade 5. Global stress and strain associated with each step are shown in the stress strain plot above.
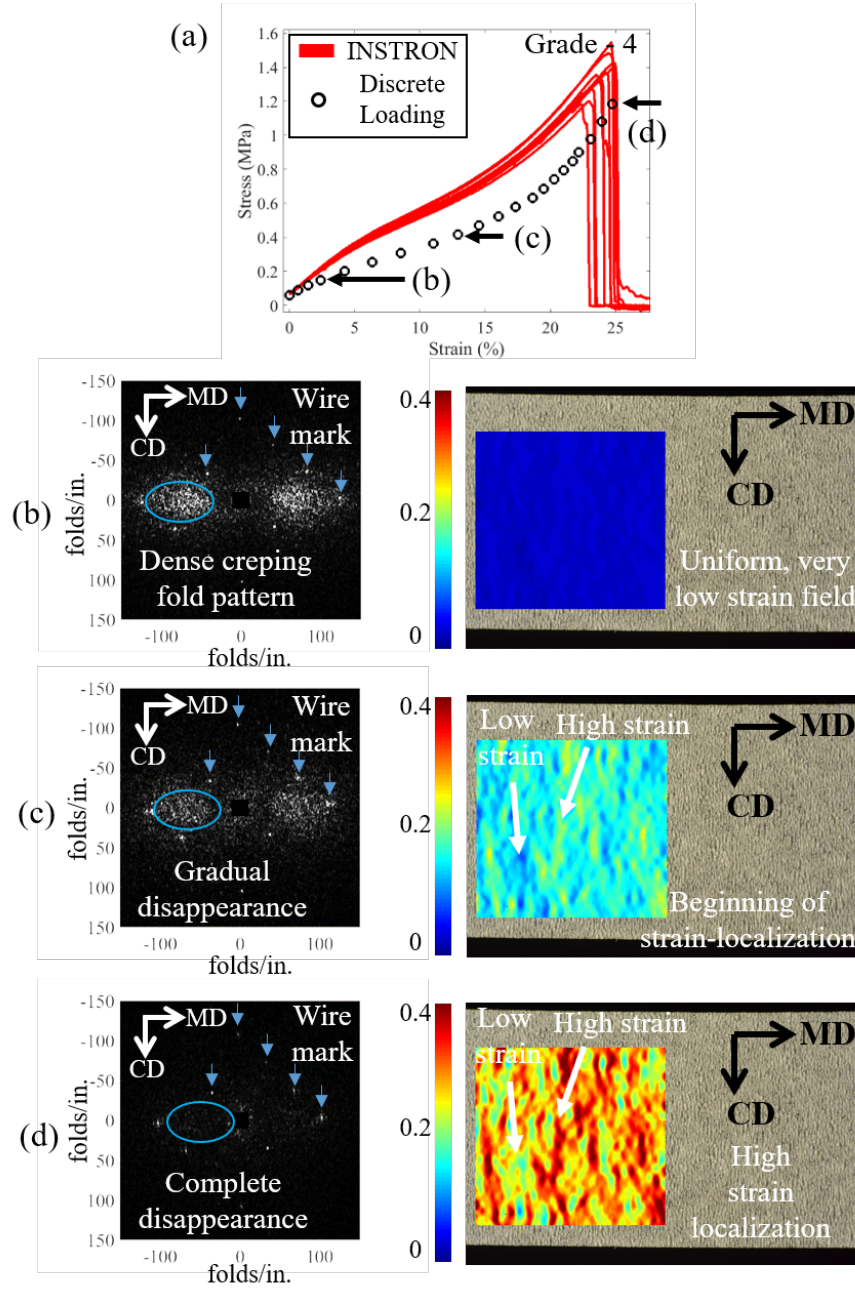
Figure 4.12: Evolution of crepe structure in 2D Fourier space (bottom left) and local principal strain field (bottom right) with increasing machine direction tensile load approximately at the end of elastic region (b), half of breaking strain (c) and at breaking strain (d) for Grade 6. Global stress and strain associated with each step are shown in the stress strain plot above.
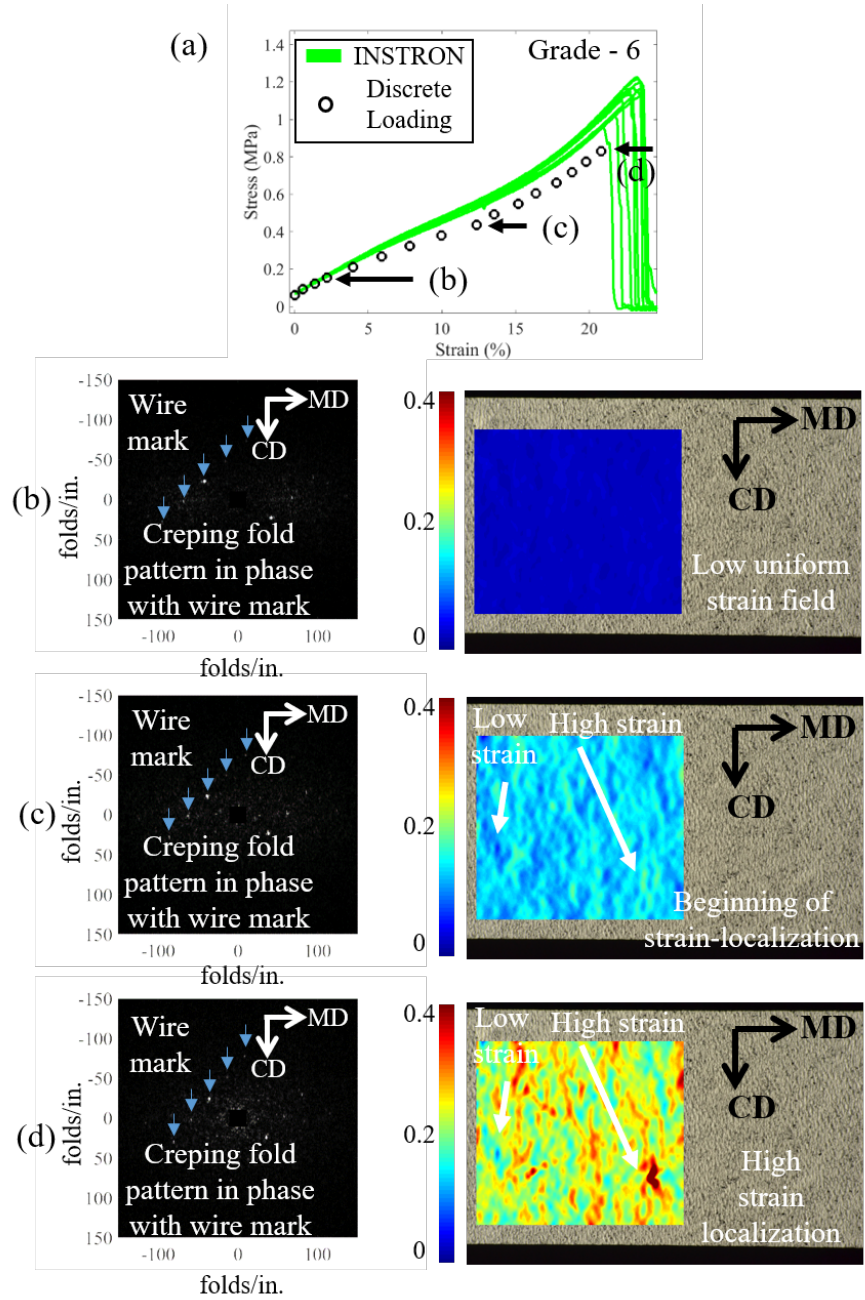
tensile load (image (b) of each figure) shows a cloud of frequency components aligned along machine direction with some other distinct frequency components spread across machine and cross direction frequency space. These distinct frequency components appear from the forming fabric induced wire mark pattern embedded in the tissue whereas the cloud of frequency along machine direction represents creping fold pattern (indicated in Fig. 4.9 (b) - Fig. 4.12 (b)). Observation of the 2D FFT just before failure (image (d) of each figure) shows that the crepe fold induced frequencies have almost disappeared, but the wire mark patterns have not. This is not very clear for grade 6 (see Fig. 4.12 (b) - (d)). Even the creping fold cloud is not well visible there. The reason is: creping folds appear almost in phase with the wire marks for Grade 6, hence the creping frequency is not well separated from the wire-mark patterns and the disappearance of the creping folds seems unclear. However, based on Grade 3-5, this study shows that the creping folds are unfolded during the tensile test governing the shape of the curve until failure. But close to failure, wire mark patterns or formation become an important structural feature because of their distinct presence.

The local strain field information at each step is extracted using two dimensional Digital Image Correlation (DIC). Digital Image Correlation is an algorithm to extract displacement and strain information at multiple points of an undeformed reference image as it is progressively deformed. A number of images of the area of interest with progressive deformation is needed. In this technique, first, the reference image is subdivided into many smaller regions (subsets) separated by some distance (subset spacing). Then the subsets are tracked down in the following deformed images based on structural similarity to extract displacements. The structural similarity generally comes from an unique speckle pattern, which is generally spray painted externally on the surface of interest. In this case, there was no additional need to spray speckle patterns on the surface. Rather the corrugated tissue surface under reflective light had enough salt and pepper patterns for the optical tracking. An opensource 2D DIC MATLAB software called Ncorr is used to perform the DIC computation. Relevant details about the DIC calculation can be found in Table 4.3.

Table 4.3: Important parameters of Digital Image Correlation analysis

Image pixel spatial resolution	8.62 μm / pixel
Subset radius	50 pixel = 431.2 μm
Subset spacing	10 pixel = 86.2 μm
Strain radius	3

Green-Lagrangian principal strain fields are obtained from the displacement fields on the tissue surface at three stages of the stress strain plot. The strain fields are plotted on the undeformed tissue surface (Fig. 4.9 (d) right Fig. 4.12 (d) right). Analysis of principal strain fields shows significant high strain localization (notice the red spots in the strain field) just before failure. Interestingly, the strain localization areas form distinct bands approximately parallel to

cross direction for all grades. The strain localization is not very distinct in Grade 5 because the sample failed prematurely before reaching the ultimate stress. Length scale of strain localization areas in all grades is in millimeter length scale which is larger than the length scale of creping folds, indicating that the reason is related to formation of the tissue. It is well known that formation of tissues change over a length scale of several millimeters. Also the regions of high strain localization start to appear from the beginning of the tensile curve, during elastic deformation (carefully notice the similar high strain pattern in (d) right and see similar bands in (b) right in all grades). These indicate that the strain localization is not the result of plastic damage entirely, but also related to the network deformation in the elastic regime, which depends on formation.

4.5 Conclusion

The experiments have provided insight into the stress-strain behaviour of creped tissue materials, especially along machine direction. The conclusions can be summarized as follows.

1. Characterization of tensile behaviour along machine direction shows initial linear elastic regime followed by a strain softening and a strain hardening before failure. This type of response is not seen in the cross-direction, which indicates that the three stage nonlinear response along machine direction is governed by the creping structures.

2. The tissue fiber network deforms significantly to accommodate large strain before failure when load is applied along machine direction. During this deformation, the inter-fiber bonds rotate and slide. This network deformation also straightens the plastically deformed, curled fibers. Straightening of fibers stiffens the tissue structure, which explains the hardening of tissue before failure in machine direction. The mechanism of failure is understood as a avalanche of bond disruption and energy release upon reaching the breaking load. However, the mechanism of deformation is not investigated along cross direction.

3. When a tensile load is applied along machine direction, the crepe folds gradually unfold and disappear, but the forming fabric induced wire mark patterns do not. Unfolding of the crepe folds explains the origin of high stretch of creped tissues along machine direction. It is understood that creping folds govern the nonlinear shape of the machine direction tensile response. However, wire mark patterns become important close to failure. Therefore it is possible that wire mark patterns affect the tensile strength.

4. Principal strain fields immediately before tensile break show significant strain localization at a length scale much larger than the crepe fold wavelength. The strain localization is related to the formation of creped tissue and distribution of creping folds.

Chapter 5

Conclusions and Future Work

5.1 Conclusions and Major Findings

Major achievements and findings of this thesis are summarized below.

1. A robust and simple surface imaging technique to quantify tissue creping structure is developed and demonstrated on a commercial tissue machine at high speeds under adverse operating conditions.

2. It is shown that the surface image based quantification of crepe structure is as accurate as cross-section imaging using, for example, SEM. The added advantages are simplicity and easier possibility of statistical analysis over a larger tissue sample for a more reliable quantification.

3. Mechanism of creping is observed at a speed over 1000 m/min on a realistic creping rig using a line laser and high speed camera. The through-thickness visualization of creping process is believed to be obtained for the first time, to our knowledge.

4. Uniaxial tensile response of tissues along machine direction is characterized by 2 transitions from linear elastic to strain softening and from strain softening to hardening before failure. No such transition exists in the cross-directional tensile response. Hence, deformation of creping folds are important to understand tensile properties of a tissue paper.

5. Microscopic, qualitative insights about tissue structure deformation are gained from machine direction tensile tests under an SEM. Tissue structure shows an exceptional capability of fiber fiber bond rotation and arrangement to accommodate the large global strain until failure. However, the role of crepe structures remain unclear from the qualitative observations.

6. Surface imaging techniques are used to understand the influence of crepe structure on the tensile response at macroscopic length scales. Creping folds are shown to govern the Young's modulus of tissue. However, formation and wire mark patterns induced by forming fabric are dominant at failure. A uniform formation is important for a more consistent tissue product.

7. Advancements in the experimental techniques made in this work are expected to be of interest to tissue manufacturers and engineers alike.

5.2   Limitations and Future Work

This work contributes to the development of experimental tools to quantify crepe structure and to understand the deformation of a tissue under load. However, many of the directions emerging from the study could not be pursued in this work and can be explored further. They have been described briefly in the sections below.

1. The crepe structure quantification techniques developed so far are limited to the extraction of creping wavelengths, but, out of plane amplitude information is also important. Further development, using photometric stereo methods for example, is needed to simultaneously measure creping wavelength and amplitude directly from surface images. Photometric stereo method works by capturing surface images under reflective light conditions from multiple angles. A camera with multiple colour sensors can be used for this purpose.

2. The proof-of-the-concept apparatus developed for online imaging can be made more robust to perform better under adverse environmental conditions, through careful engineering design. It is possible for this set-up to traverse the surface of the tissue by to and fro movement along cross direction of the web on a tissue machine.

3. Much work remains to be done to understand the *shape* of nonlinear tensile response, specifically along the machine direction. Here, a combined numerical and experimental techniques have to be pursued.

4. The importance of forming fabric induced wire mark patterns remains to be fully understood. Our results clearly point to the influence of wire mark patterns on the tensile response. Such pre-patterned base sheets before creping are also common to base sheets produced by Through-Air-Drying (TAD). A systematic study of different wire mark patterned base sheet before and after creping can be pursued in future.

5. Blade wear is known to play an important role during creping. A systematic study of temporal variation of the crepe structure and its distribution can be done to understand the impact of blade wear on the physics of creping.

Bibliography

[1] K. Pan, R. Das, A. S. Phani, and S. Green, "An elastoplastic creping model for tissue manufacturing," *International Journal of Solid and Structures*, no. IJSS-D-18-00836, Under review.

[2] *PN-EN ISO 12625-4:2016 Tissue paper and tissue products – Part 4: Determination of tensile strength, stretch at maximum force and tensile energy absorption.* 2016.

[3] M. Ramasubramanian, "Physical and mechanical properties of towel and tissue," in *Handbook of Physical Testing of Paper*, pp. 683–896, CRC Press, 2001.

[4] H. Hollmark, "Mechanical properties of tissue," vol. 1, pp. 497–521, 1983.

[5] H. Hollmark, "Study of the creping process on an experimental paper machine," *STFI-meddelande, Serie B*, no. 144, 1972.

[6] J. F. Oliver, "Dry-creping of tissue paper-a review of basic factors," *Tappi*, vol. 63, no. 12, pp. 91–95, 1980.

[7] K. Pan, A. S. Phani, and S. Green, "Particle dynamics modeling of the creping process in tissue making," *Journal of Manufacturing Science and Engineering*, vol. 140, no. 7, p. 071003, 2018.

[8] W. McConnel, "The science of creping," *Tissue World Americas, Miami Beach, FL*, 2004.

[9] M. K. Ramasubramanian and D. L. Shmagin, "An experimental investigation of the creping process in low-density paper manufacturing," *Journal of Manufacturing Science and Engineering*, vol. 122, no. 3, pp. 576–581, 2000.

[10] M. K. Ramasubramanian, Z. Sun, and G. Chen, "A mechanics of materials model for the creping process," *Journal of Manufacturing Science and Engineering*, vol. 133, no. 5, p. 051011, 2011.

[11] S. S. Gupta, "Study of delamination and buckling of paper during the creping process using finite element method-a cohesive element approach.," *Ph.D. Thesis, North Carolina State University, Raleigh, NC*, 2013.

[12] D. M. Rasch, T. A. Hensler, and D. J. Daniels, "A papermaking belt," July 11 1995. US Patent 5,431,786.

[13] H. Ihalainen, K. Marjanen, M. Mäntylä, and M. Kosonen, "Developments in camera based on-line measurement of paper," in *PaperCon 2012 Growing the Future, Control Systems 2012 , April 22-25, New Orleans, Louisiana, USA*, PaperCon, TAPPI, 2012.

[14] C. Crosby, A. Eusufzai, R. Mark, R. Perkins, J. Chang, and N. Uplekar, "A digitizing system for quantitative measurement of structural parameters in paper," *Tappi*, vol. 64, no. 3, pp. 103–106, 1981.

[15] J. Sabater, J. C. Kerneis, and S. Bauduin, "Device for the continuous determination of a surface state index for a moving creped sheet," Dec. 18 1990. US Patent 4,978,861.

[16] W. A. Von Drasek, S. L. Archer, and G. S. Furman Jr, "Method and apparatus to monitor and control sheet characteristics on a creping process," Dec. 26 2017. US Patent 9,851,199.

[17] J. P. Raunio, "Quality characterization of tissue and newsprint paper based on image measurements; possibilities of on-line imaging," *Thesis for the degree of Doctor of Science in Technology, Tampere University of Technology*, 2014.

[18] M. Kellomäki and A. Paavola, "Apparatus and method for measuring caliper of creped tissue paper based on a dominant frequency of the paper and a standard deviation of diffusely reflected light including identifying a caliper measurement by using the image of the paper," Apr. 5 2016. US Patent 9,303,977.

[19] H. L. Cox, "The elasticity and strength of paper and other fibrous materials," *British Journal of Applied Physics*, vol. 3, no. 3, pp. 72–79, 1952.

[20] D. H. Page, R. S. Seth, and J. H. De Grace, "The elastic modulus of paper. i. the controlling mechanisms," *Tappi*, vol. 62, no. 9, pp. 99–102, 1979.

[21] D. H. Page and R. S. Seth, "The elastic modulus of paper. ii. the importance of fiber modulus, bonding, and fiber length," *Tappi*, vol. 63, no. 6, pp. 113–116, 1980.

[22] D. H. Page and R. S. Seth, "The elastic-modulus of paper. iii. the effects of dislocations, microcompressions, curl, crimps, and kinks," *Tappi*, vol. 63, no. 10, pp. 99–102, 1980.

[23] R. S. Seth and D. H. Page, "The stress-strain curve of paper," *The Role of Fundamental Research in Paper Making, Trans. VIIth Fund. Res. Symp. Cambridge*, vol. 1, pp. 421–452, 1981.

[24] S. Borodulina, A. Kulachenko, M. Nygårds, and S. Galland, "Stress-strain curve of paper revisited," *Nordic Pulp & Paper Research Journal*, vol. 27, no. 2, pp. 318–328, 2012.

[25] H. F. Rance, "The formulation of methods and objectives appropriate to the rheological study of paper," *Tappi*, vol. 39, no. 2, pp. 104–115, 1956.

[26] G. J. Williams and J. G. Drummond, "Preparation of large sections for the microscopical study of paper structure," *Journal of Pulp and Paper Science*, vol. 26, no. 5, pp. 188–193, 2000.

[27] A. Hagman and M. Nygårds, "Investigation of sample-size effects on in-plane tensile testing of paperboard," *Nordic Pulp & Paper Research Journal*, vol. 27, no. 2, pp. 295–304, 2012.

[28] D. Caulfield, "Effect of moisture and temperature on the mechanical properties of paper," *Solid Mechanics Advances in Paper Related Industries*, pp. 50–62, 1990.

[29] D. Roylance, P. McElroy, and F. McGarry, "Viscoelastic properties of paper," *Fibre Science and Technology*, vol. 13, no. 6, pp. 411–421, 1980.

[30] T. Uesaka, K. Murakami, and R. Imamura, "Two-dimensional linear viscoelasticity of paper," *Wood Science and Technology*, vol. 14, no. 2, pp. 131–141, 1980.

Appendix A

Microtensile Stage Extension Rate Calibration

The extension rate controller of the microtensile stage was not calibrated during the tensile tests. It was discovered later during data analysis and a calibration factor had to be multiplied with the apparent extension rate to correct it. The calibration factor was calculated by measuring the actual relative rate of separation of the jaws while the apparent extension rate was kept fixed at 1 mm/min from the software. The relative jaw separation was optically tracked with time for over 3 minutes. The initial and final configurations of the microtensile stage are shown in Fig. A.1 (left). A series of images were taken in between and analyzed to extract the jaw separation with time; the rate was calculated from the data (see A.1 (right)). The actual extension rate was found to be 1.589 mm/min. Therefore the extension rate calibration factor was 1.589.

During the previous tensile tests , the apparent extension rate was set to be 1.5 mm/min from the software. Therefore, the actual extension rate was 2.37 mm/min (multiply 1.5 with the 1.589).
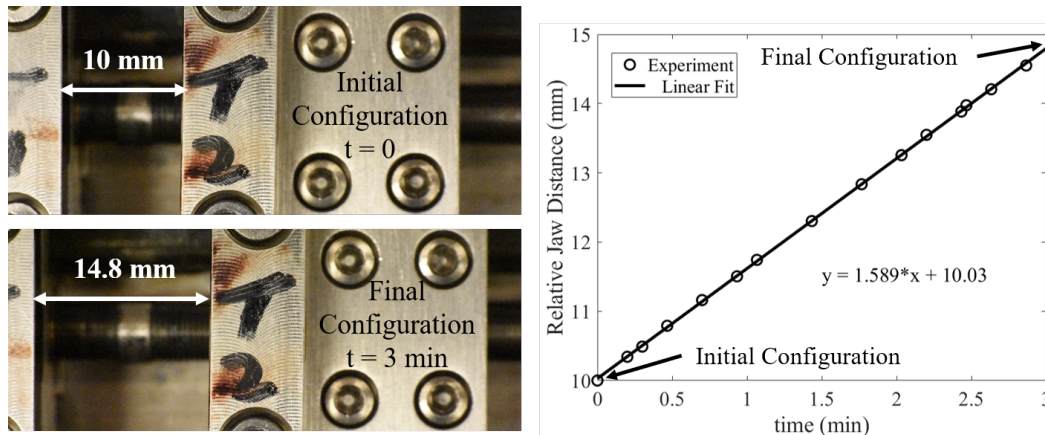

Figure A.1: Microtensile stage extension rate calibration methodology. A series of image is taken at regular intervals between the initial (left top) and final (left bottom) configuration of the stage. The relative distance between the jaws is plotted against time (see right). The extension rate is calculated from the slope of the linear fit line.